Chemistry–A European Journal
Research Article
doi.org/10.1002/chem.202400781
Chemistry Europe
European Chemical Societies Publishing
www.chemeurj.org

Structure and Solution Behavior of Rare-Earth-Metal Complexes with Tripodal *N*-Donor Ligands

Perrine M. R. Wingering,[a] Felix Krämer,[a] Melina E. A. Dilanas,[a] Cristina Ruiz-Martínez,[b] Ignacio Fernández,*[b] and Frank Breher*[a]

Introduction

The coordination chemistry of trivalent *f*-block elements with *N*-donor ligands is of great interest because it applies in nuclear waste treatment.[1] For instance, the SANEX process utilizes *N*-donor ligands containing bis-triazinyl-pyridine (BTP) or bis-triazinyl-bipyridine (BTBP) moieties to separate Am(III) and Cm(III) from lanthanides.[2] However, the separation of 4*f* and 5*f* elements represents a challenge due to their chemical similarities. Exploring the coordination chemistry of lanthanides and actinides can provide insight into the key properties influencing selective coordination, such as steric effects, bond length and stoichiometry.[3]

In our previous work, the coordination of multiple rare-earth elements (REE) with different κ^6*N*-coordinating, podant donor ligands with tris(hydrazonyl)thiophosphanyl units as linker (SP-ligands, see Scheme 1) have been explored.[4,5] The complexation behaviour of these polydentate nitrogen ligands was investigated in detail by X-ray single–crystal structure analysis in the solid state and by different NMR techniques in solution. ^{19}F NMR low temperature NMR experiments, ^{89}Yttrium NMR as well as PGSE-NMR measurements have enabled the evaluation of the degree of ion pairing in solution. The geometrical investigations and calculation of the steric maps have permit to evaluate the flexibility and steric bulk of each ligand. Additionally, the donor abilities of the ligands have been explored by DFT calculations and cyclic voltammetry. Finally, competition studies have been performed and revealed that there is a correlation between donor strength and selectivity of complexation.

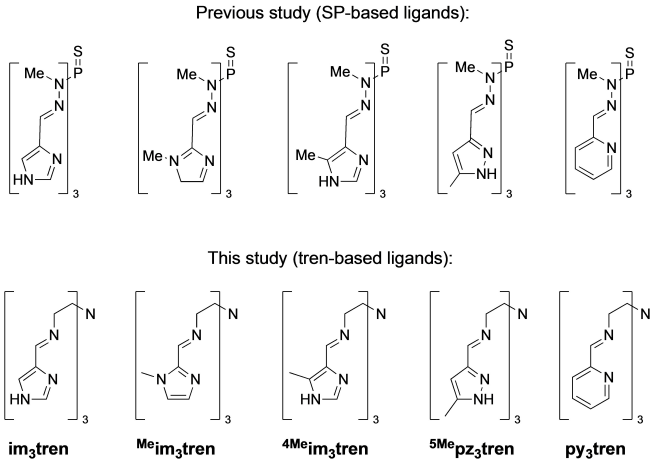

Scheme 1. κ^6*N* donor ligands of our previous study and the ligands investigated in this study. Some of the ligands have been reported previously.[7–10]

Based on the podant κ^6*N* tripodal ligands functionalized with different *N*-heterocycles, a new family of ligands consisting of a tren anchoring unit was synthetized (Scheme 1). Compared to the previously studied set of ligands, the SP-linker part has been replaced by a tris(2-aminoethyl) amine moiety (tren). The aim was to explore a ligand system still featuring a rigid tripodal structure, but also following the so-called "CHON principle".[6] This means that the ligands only contain elements such as carbon (C), hydrogen (H), oxygen (O) and nitrogen (N), which enable all chemical reagents to be converted into gases through combustion that can be released into the environment easily and safely.

Herein, we present the synthesis of a new family of κ^n*N* (n = 6, 7) donor ligands and their complexation with several Ln^{3+} ions. The obtained complexes were characterized using techniques such as X-ray diffraction, pulsed field–gradient spin echo (PGSE) diffusion NMR measurement and multinuclear NMR spectroscopy. As in our previous work, the donor strengths of the ligands were investigated by DFT calculations and by cyclic voltammetry by using the synthetized cerium complexes. Competition studies were performed to investigate the correlation between donor ability and selectivity.

[a] P. M. R. Wingering, F. Krämer, M. E. A. Dilanas, F. Breher
Institute of Inorganic Chemistry, Karlsruhe Institute of Technology (KIT), Engesserstr. 15, 76131 Karlsruhe, Germany
E-mail: breher@kit.edu

[b] C. Ruiz-Martínez, I. Fernández
Department of Chemistry and Physics, Research Centre CIAIMBITAL, University of Almería, Ctra. Sacramento s/n, 04120 Almería, Spain
E-mail: ifernan@ual.es

Supporting information for this article is available on the WWW under https://doi.org/10.1002/chem.202400781

Results and Discussion

Synthesis

The synthesis of **im$_3$tren**,[7–9] **^{Me}im$_3$tren**,[7] **^{4Me}im$_3$tren**[7] and **py$_3$tren**[10] have been reported previously by the groups of W. R. Scheidt, M. Kojima and P. G. Plieger. Following similar conditions, the synthesis of the **^{5Me}pz$_3$tren** was performed by imine condensation between the tris(2-aminoethyl) amine (tren) precursor and the corresponding *N*-heterocyclic aldehyde (Scheme 2). The formation of the ligand was proved by disappearance of the aldehyde signal (δ_H = 9.5–10.5 ppm) in the proton NMR spectrum. Complexation with the different Ln(OTf)$_3$ salts (Ln=Y, La, Ce, Sm and Lu) has been performed by stirring a solution of the ligand and the desired lanthanide triflate in a stoichiometric ratio of 1:1 at room temperature overnight. The solvent used for complexation was varying from THF to methanol, depending on the solubility of the ligands (see Experimental Section). The complexations of REE with large (La and Ce), middle (Sm) and small (Lu and Y) ionic radii were successful, and the complexes were obtained in variable isolated yields of 5–75%.

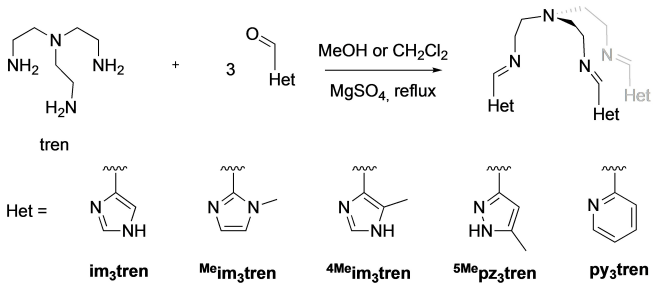

Scheme 2. Synthesis of the ligands. Some of the ligands have been reported previously.[7–10]

Solid State Structures

The solid-state structures of the complexes are very similar and represent mononuclear species. The cationic metal centres are in most cases coordinated by two triflate counter ions (κ^1O) and by the apical, imine and heterocyclic nitrogen atoms of the ligand (κ^7N). The only exception is observed for **La(^{Me}im$_3$tren)** and **Ce(^{Me}im$_3$tren)**, with the metal atoms coordinated with all three triflate counter ions (κ^1O), the imine, and heterocyclic nitrogen atoms (κ^6N) of the tripodal ligand. Selected bond lengths are summarized in Table 1.

For the **M(^{Me}im$_3$tren)** complexes (M = La and Ce), all triflate counter ions are coordinated to the metal centres but the apical nitrogen atoms are not coordinated. As expected, the La–N bond lengths are longer than the Ce–N bond lengths (average:

Table 1. Selected bond lengths (Å).

Compound	La(im$_3$tren)	La(^{Me}im$_3$tren)	Ce(^{Me}im$_3$tren)	Y(^{4Me}im$_3$tren)	Ce(^{4Me}im$_3$tren)
M–N1	3.035(3)	–	–	2.6528(18)	2.735(7)
M–N2	2.670(3)	2.686(2)	2.662(7)	2.4912(18)	2.611(6)
M–N3	2.710(3)	2.753(2)	2.657(7)	2.5406(19)	2.590(6)
M–N4	2.645(3)	2.725(2)	2.720(7)	2.4566(17)	2.588(7)
M–N5	2.671(3)	2.660(2)	2.711(7)	2.4565(17)	2.611(8)
M–N7	2.664(3)	2.704(3)	2.624(7)	2.5014(18)	2.619(7)
M–N9	2.680(3)	2.723(3)	2.681(8)	2.5361(17)	2.585(6)
M–O10	2.611(3)	2.566(2)	2.553(6)	2.4723(15)	2.555(5)
M–O20	2.618(3)	2.582(2)	2.567(6)	2.4348(15)	2.548(5)
M–O30	–	2.669(2)	2.612(6)	–	–
coord. number	7	6	6	7	7
Compound	Sm(^{4Me}im$_3$tren)	Ce(^{5Me}pz$_3$tren)	Y(py$_3$tren)	La(py$_3$tren)	Ce(py$_3$tren)
M–N1	2.694(3)	2.974(4)	2.604(3)	2.9945(13)	2.9880(19)
M–N2	2.532(3)	2.661(4)	2.447(3)	2.6600(13)	2.7081(19)
M–N3	2.572(3)	2.694(5)	2.479(3)	2.7258(13)	2.6268(18)
M–N4	2.518(3)	2.654(4)	2.503(3)	2.6474(12)	2.6341(19)
M–N5	2.515(3)	2.647(4)	2.624(3)	2.7578(13)	2.8080(19)
M–N7	2.567(3)	2.709(4)	2.583(3)	2.8231(13)	2.819(2)
M–N9	2.575(3)	2.718(5)	2.585(3)	2.8326(13)	2.7356(19)
M–O10	2.501(2)	2.455(3)	2.375(3)	2.5196(11)	2.4984(15)
M–O20	2.524(2)	2.484(4)	2.387(3)	2.4909(12)	2.4670(16)
M–O30	–	–	–	–	–
coord. number	7	7	7	7	7

Research Article
doi.org/10.1002/chem.202400781
Chemistry Europe
European Chemical Societies Publishing

Ø(La–N) = 2.709 Å and Ø(Ce–N) = 2.675 Å), due to the larger ionic radius of La^{3+} compared to Ce^{3+} (La^{3+}: 121.6 pm and Ce^{3+} :119.6 pm).[11] The same trend is observed for the M–O bond lengths (Ø(La–O) = 2.606 Å and Ø(Ce–O) = 2.577 Å).

The decrease of bond lengths with decreasing ionic radius is also observed in the **M(4Meim3tren)** complexes series (M = Y, Ce, Sm). The shorter bonds are the Y–N bonds with Ø 2.168 Å, followed by Sm–N with Ø 2.568 Å and Ce–N with Ø 2.620 Å. For the M–O bond lengths the same trend is observed: Y–O, Ø = 2.454 Å, Sm–N, Ø = 2.513 Å and Ce–N, Ø 2.552 Å.

For the **M(py3tren)** complex series, a structural difference is observed. For **La(py3tren)** and **Ce(py3tren)**, two triflate counter ions are coordinated to the metal cation in equatorial position and a solvent molecule (acetonitrile) is coordinated in axial position. Here, the binding of a solvent molecule in axial position is not influencing the coordination of the axial nitrogen atom and the apical nitrogen atoms are also coordinated to the metal centre (κ^7N). On the contrary, the coordination of the axial triflate counter ion in **La(Meim3tren)** and **Ce(Meim3tren)** obviously has an influence on the coordination of the apical nitrogen. For the bond lengths, the same trend as for the other complex series is followed. The La–N and Ce–N bond lengths are comparable (Ø(La–N) = 2.741 Å and Ø(Ce–N) = 2.722 Å) and the Y–N bond lengths are much shorter (Ø(Y–N) = 2.537 Å). The same trend is observed for the M–O bond lengths (Ø(La–O) = 2.505 Å, Ø(Ce–O) = 2.483 Å and Ø(Y–O) = 2.381 Å).

For the ligand systems **(im3tren)** and **(5Mepz3tren)**, only one crystal structure could be obtained for each ligand. For **La(im3tren)**, the obtained La–N bond lengths (Ø(La–N) = 2.673 Å) and La–O bond lengths (Ø(La–O) = 2.615 Å) are comparable with the one obtained for the other lanthanum complexes. Similarly to **La(py3tren)**, a solvent molecule (acetonitrile) is coordinated to the La centre in axial position for **La(im3tren)**.

The crystal structure of **Ce(5Mepz3tren)** is similar to the crystal structure of **Ce(py3tren)**; only two triflate counter ions are coordinated to the cerium centre, the apical nitrogen atom is also coordinated and in axial position a solvent molecule is coordinated to the cerium cation. The bond lengths (Ø(Ce–N) = 2.681 Å and Ø(Ce–O) = 2.470 Å) are in the range expected in comparison with the crystal structure from the other cerium complexes shown previously.

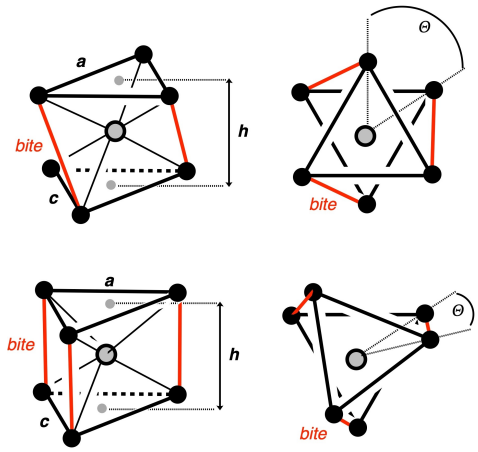

Figure 1. Selected geometric measures for complexes of tris-bidentate ligands; (top) for the case of the ideal octahedron; (bottom) for the ideal trigonal prismatic structure; *h*: height of the polyhedron (here distance of the planes defined by $(N_{imin})_3$ and $(N_{het})_3$); *a*: non-bonded distance of N_{imin} donors; *c*: non-bonded distance of N_{het} donors; *bite*: intra-podal donor distance; *θ*: trigonal twist angle of the planes $(N_{imin})_3$ and $(N_{het})_3$.[13]

All the lanthanide complexes characterized by X-ray diffraction possess bond lengths in the expected range.[12] For the previously reported SP-ligands, all the triflate counter ions were coordinated to the metal centre (κ^1O) with three imine and three heterocyclic nitrogen atoms (κ^6N).[4] The here reported complexes display the same coordination manner for the *N*-donor ligand units with additional coordination of the apical nitrogen atom (κ^7N), however only two triflate counter ions are coordinating to the cationic metal centre. The only exception is observed for **La(Meim3tren)** and **Ce(Meim3tren)** where all three triflate anions are coordinating.

To verify if these structural differences are due to varying steric profile and to quantify the ligand "pockets" of **im3tren**, **Meim3tren**, **4Meim3tren**, **5Mepz3tren** and **py3tren**, analysis of selected geometric parameters (Figure 1) have been executed and are reported in Table 2. The average values of the different

Table 2. Selected structural details for the cerium complexes (cf. Figure 1).

	La(im3tren)	Ce(Meim3tren)	Ce(4Meim3tren)	Ce(5Mepz3tren)	Ce(py3tren)
Ø *d*(Ce–N_{tren})/Å	3.0349	3.1067	2.7353	2.9739	2.9880
Ø *d*(Ce–N_{imin})/Å	2.6750	2.6797	2.5964	2.6702	2.6563
Ø *d*(Ce–N_{het})/Å	2.6474	2.6718	2.6051	2.6915	2.7876
h[a]/Å	2.3527	2.3046	2.7304	2.3689	2.3733
h_1[b]/Å	1.3287	1.3827	1.0929	1.2922	1.2996
h_2[b]/Å	1.0825	0.9873	1.6431	1.1372	1.1431
bite[a]/Å	2.7401	2.7786	2.7725	2.7335	2.7539
a[a]/Å	3.9229	3.8657	3.9843	3.9330	3.9128
c[a]/Å	3.8861	3.9283	3.4771	4.3582	4.1780
Θ[a]/°	62.493	62.601	64.423	61.300	60.722

[a] according to Figure 1; [b] h_1 and h_2 denote the distance of the central metal ion from the planes defined by $(N_{imin})_3$ and $(N_{het})_3$, respectively.

bond lengths between the cerium centre and the N_{tren}, N_{imin} and N_{het} are given, as well as the non-bonded distances between the N_{imin} and N_{het} atoms. In addition, the distance between the N_{imin} and the N_{het} plane (h) has been reported together with the distance of the planes to the metal centre (h_1 and h_2). Furthermore, the distortion angle has been determined (Θ).[13] The cerium complexes have been chosen for this study, only for **im$_3$tren**, the **La(im$_3$tren)** was used because **Ce(im$_3$tren)** could not be characterized by XRD. Considering the bond lengths between the cerium centre and the different nitrogen atoms of the ligand, **Ce(^{4Me}im$_3$tren)** displays drastically shorter bond lengths compared to the other complexes. The Ce^{3+} ion appears to be effectively encapsulated by the ligands and therefore no axial counter ion or solvent molecule can coordinate to the metal centre. Furthermore, **Ce(^{4Me}im$_3$tren)** shows the highest trigonal distortion ($\Theta = 64.423°$) and the highest h value ($h = 2.7304$ Å), which attest to the higher flexibility of the ligand. For **Ce(^{5Me}pz$_3$tren)**, the longest non-binding N_{het} distances are observed, most likely due to the steric hinderance created by the methyl groups of the pyrazole rings. The ligand system seems to be more opened on the bottom and has a more conical geometry. The three other complexes **La(im$_3$tren)**, **Ce(^{Me}im$_3$tren)** and **Ce(py$_3$tren)** display similar structures and no particular structural parameters have been observed. In comparison with the results obtained for the SP-ligands in our previous study, the h_1 values are significantly lower for the tren-ligands (Ø h_1(tren) = 1.279 Å and Ø h_1(SP) = 2.062 Å) and the h_2 values are higher (Ø h_2 (tren) = 1.199 Å and Ø h_2 (SP) = 0.528 Å), which testify that the cerium centre is inserted more deeply into the tren-ligand system in comparison to the SP-ligands.[4] This deep increment is possibly supported by the coordination of the apical nitrogen atom N_{tren}. It could explain why the coordination of an axial triflate counter ion is more unfavoured. Moreover, **Ce(^{Me}im$_3$tren)** displays the higher h_1 (1.3827 Å) and the lower h_2 value (0.9873 Å) and is the complex in which the cation is less profound into the ligand system. Therefore, **^{Me}im$_3$tren** is the ligand which best enables the coordination of the axial triflate counter ion.

Additionally, the steric bulk has been evaluated qualitatively by analysing the steric maps of these different complexes.[14] The steric maps of the complexes are shown in Figure 2 and are viewed from the Ce–N_{tren} axis.

For clarity reasons, the axial substituents have been deleted when present. For **Ce(^{4Me}im$_3$tren)** (c), the steric hinderance at the cerium centre is enormous compared to the other steric maps. Thereby, the coordination of the third triflate counter ion or a solvent molecule is hindered by the steric bulk of the ligand. For **Ce(^{5Me}pz$_3$tren)** (d), the methyl groups of the ligand fill up the coordination sphere of the cerium atom toward the Ce–N_{tren} axis. The third triflate counter ion is probably too sterically demanding to coordinate to the cerium centre. However, there is enough space for an acetonitrile molecule to coordinate. **La(im$_3$tren)** (a) and **Ce(py$_3$tren)** (e) display comparable steric hindrances at the lanthanide centre. For **Ce(^{Me}im$_3$tren)** (b), the cerium centre seems to be less crowded as for the other complexes, which explains why the third triflate counter ion is coordinated in axial position. Compared to the previously reported SP-ligands, the steric maps display much more steric bulk for the tren-ligands, what explains why the coordination of the axial triflate counter ion is more challenging. The gain on flexibility caused an enhanced encapsulation of the lanthanide ions into the ligand system, which could lead to higher coordination facility.

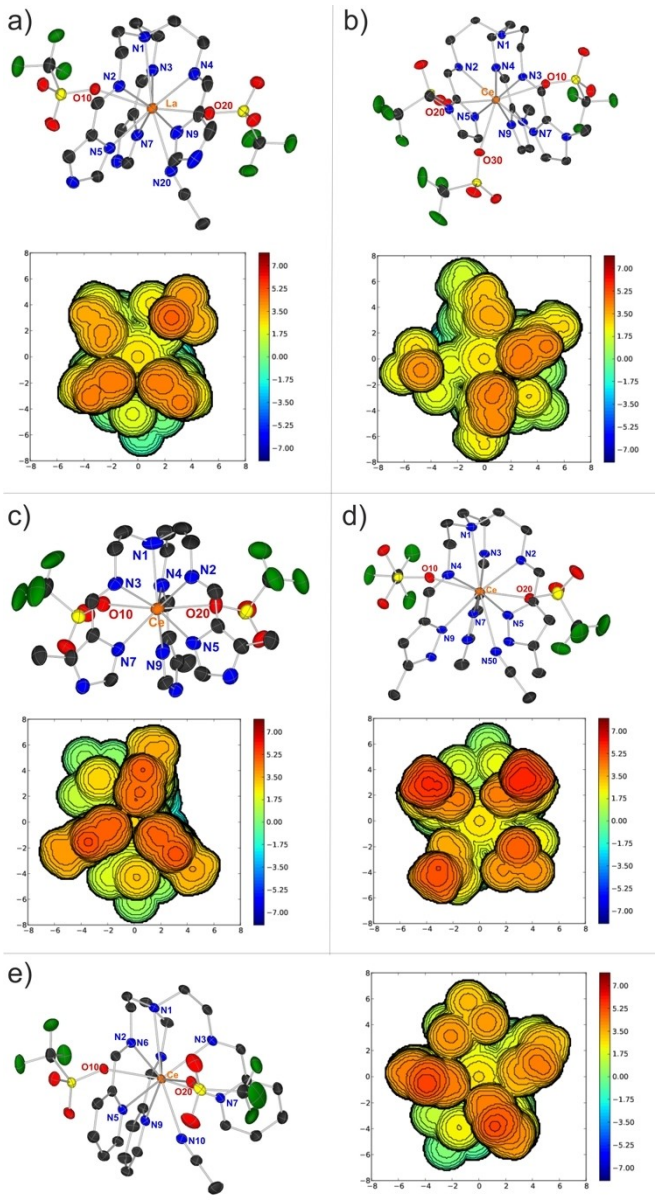

Figure 2. Molecular structures of selected [(Het)M^{III}] complexes and the associated calculated steric maps using SambVca.[15] Views are given from below omitting the lowest triflate anions (O30): core structures [La(im$_3$tren)(NCMe)(OTf)$_2$]$^+$ of **La(im$_3$tren)** (a), [Ce(^{Me}im$_3$tren)(OTf)$_3$] of **Ce(^{Me}im$_3$tren)** (b), [Ce(^{4Me}im$_3$tren)(OTf)$_2$]$^+$ of **Ce(^{4Me}im$_3$tren)** (c), [Ce(^{5Me}pz$_3$tren)(NCMe)(OTf)$_2$]$^+$ of **Ce(^{5Me}pz$_3$tren)** (d), and [Ce(py$_3$tren)(NCMe)(OTf)$_2$]$^+$ of **Ce(py$_3$tren)** (e). Thermal ellipsoids are given at the 30 % probability level. Hydrogen atoms are omitted for clarity.

Diffusion NMR Experiments

As can be seen in the crystal structures of the title compounds, only two triflate counter ions are coordinated to the metal centre in equatorial position. The coordination of the third triflate group in axial position is observed only for **La(Meim$_3$tren)** and **Ce(Meim$_3$tren)** in the solid state.

However, for all synthesized compounds, only one sharp signal is observed in the ^{19}F NMR spectra (see Supporting Information, Section S3), what testifies a fast exchange of the triflate groups at room temperature, although with some minor differences in terms of chemical shift that could be correlated with the degree of ion pairing (see below). To investigate this behaviour in more detail and to quantify the degree of ion-pairing in solution, PGSE (pulsed gradient spin echo) NMR experiments were conducted.[16] ^{1}H and ^{19}F NMR diffusion experiments were performed for all Y, La and Lu complexes, the cationic (D_C) and anionic (D_A) diffusion constants, hydrodynamic radius (r_H),[17] and the D_C/D_A quotient are given in Table 3.

Full coordination is observed for $D_C/D_A = 1$ and a deviation from the unity value is an indication for some degree of solvent-separated ion-pairs (SSIPs). The results obtained have been documented in Table 3 and visually represented in Figure 3. All D_C/D_A values deviate from 1, strongly indicating an exchange between coordinated and free triflates. For the lutetium complexes, the D_C/D_A values demonstrate a narrow range of 0.62 to 0.69. However, in the cases of lanthanum and yttrium, the ion-pairing ratios exhibit not only broader ranges but also larger values, spanning from 0.64 to 0.89 and 0.66 to 0.84, respectively. These outcomes can be attributed to the smaller ionic radius of the Lu^{3+} cation (Lu^{3+}: 103.2 pm) in comparison to Y^{3+} and La^{3+} (Y^{3+}: 107.5 pm, La^{3+}: 121.6 pm).[11] The observed trends reveal a singular exception with **im$_3$tren**, where the yttrium complex displays a slightly lower ion pairing of 0.66. As we will discuss further below, this exception remains consistent when other spectroscopic features are considered. Additionally, the graphical representation reveals two distinct trends. In the cases of im$_3$tren and py$_3$tren, the lanthanum complexes exhibit a higher degree of ion-pairing compared to their yttrium analogues, which is reversed for the substituted *N*-heterocyclic ligands **Meim$_3$tren**, **4Meim$_3$ten**, and **5Mepz$_3$tren**. For lanthanum and lutetium, a consistent correlation is deduced between ionic radius and ion-pairing regardless of the specific ligand considered. This correlation is evident as the D_C/D_A value diminishes proportionately with the decrease in ionic radius. Intriguingly, this correlation does not persist in the case of yttrium. Therefore, a comprehensive discussion based on ^{13}C, ^{19}F, and ^{89}Y NMR analyses is presented in the subsequent section to address this deviation. Besides, a low ion-pairing is observed for **La(Meim$_3$tren)** ($D_C/D_A = 0.64$) and **La(4Meim$_3$tren)** ($D_C/D_A = 0.65$), which are the lowest obtained for all the lanthanum complexes. The latter is consistent with the X-ray structure of its analogue **Ce(4Meim$_3$tren)**, in which only two triflates are bound to the metal and a significant steric bulk around the metal centre is observed in the steric map. In the case of the former, its solid-state structure shows how the third triflate group is coordinating to the lanthanum centre and therefore a high degree of ion-pairing should be expected in solution, which is not observed. Overall, the tren-ligands seem to be more flexible than the SP-ligands, as the structural parameters h_1 and h_2 have shown in the previous section. It was expected that the higher flexibility of the ligands system provides more space around the cationic centre to enable coordination of more counter ions or bigger lanthanides. However, this flexibility did not result in the coordination of the third triflate group in most of the cases, probably due to the partial coordination of the apical nitrogen N_{tren} that lead to a higher encapsulation of the cationic centre.[18]

Table 3. Diffusion coefficient D and hydrodynamic radius r_H for selected complexes (each 30 mM solution in CD_3CN at 292 K).

Compound		Nucl.	$D/10^{-10}$ m^2/s [a]	r_H/Å[b]	D_C/D_A
M(im$_3$tren)	Y	^{1}H	11.64	5.3	0.66
		^{19}F	17.68	4.0	
	La	^{1}H	11.65	5.3	0.70
		^{19}F	16.63	3.7	
	Lu	^{1}H	12.15	5.1	0.67
		^{19}F	18.02	3.4	
M(Meim$_3$tren)	Y	^{1}H	12.14	5.1	0.75
		^{19}F	16.21	3.8	
	La	^{1}H	12.49	4.9	0.64
		^{19}F	19.64	3.1	
	Lu	^{1}H	12.17	5.0	0.63
		^{19}F	19.33	3.2	
M(4Meim$_3$tren)	Y	^{1}H	11.46	5.3	0.71
		^{19}F	16.15	3.8	
	La	^{1}H	10.47	5.9	0.65
		^{19}F	16.03	3.8	
	Lu	^{1}H	12.08	5.1	0.62
		^{19}F	19.40	3.2	
M(5Mepz$_3$tren)	Y	^{1}H	12.20	5.0	0.84
		^{19}F	14.42	4.3	
	La	^{1}H	12.25	5.0	0.79
		^{19}F	15.52	4.0	
	Lu	^{1}H	12.89	4.8	0.69
		^{19}F	18.68	3.3	
M(py$_3$tren)	Y	^{1}H	12.77	4.8	0.78
		^{19}F	16.29	3.8	
	La	^{1}H	12.49	4.9	0.89
		^{19}F	14.00	4.4	
	Lu	^{1}H	12.51	4.9	0.68
		^{19}F	18.38	3.4	

[a] experimental error ±2%; [b] calculated from the diffusion coefficient by Stokes–Einstein equation, viscosity $\eta = 0.363\ 10^{-3}$ kg m^2 s^{-2}.[17]

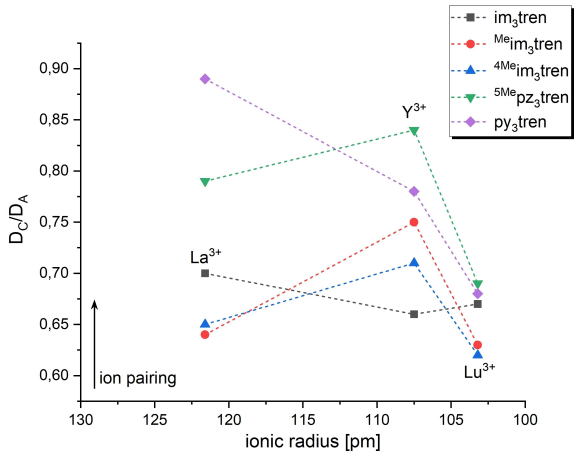

Figure 3. Variation of the ratio D_C/D_A as a function of ionic radius (in pm) of the central metal ion in CD_3CN at 292 K (D_C/D_A = quotient of the diffusion coefficient of cationic and anionic species, c = 40 mM).

Table 4. Experimental and computed ^{89}Y NMR chemical shifts.

Compound	Exp.[b] ^{89}Y NMR/ppm	Calcd.[c] ^{89}Y NMR/ppm	Calcd.[d] ^{89}Y NMR/ppm
Y(im$_3$tren)	131.3	−16.2	−26.2
[Y(im$_3$tren)-X]$^+$[a]	–	101.7	94.8
Y(^{Me}im$_3$tren)	78.9	−7.2	−17.1
[Y(^{Me}im$_3$tren)-X]$^+$[a]	–	128.5	117.7
Y(^{4Me}im$_3$tren)	154.7	135.6[e]	125.5[e]
[Y(^{4Me}im$_3$tren)-X]$^+$[a]	–	94.4	81.8
Y(^{5Me}pz$_3$tren)	45.3	73.8[e]	62.0[e]
[Y(^{5Me}pz$_3$tren)-X]$^+$[a]	–	83.9	69.0
Y(py$_3$tren)	75.8	75.6[f]	67.0[f]
[Y(py$_3$tren)-X]$^+$[a]	–	27.3	17.9

[a] complexes with two coordinated triflates and one acetonitrile; [b] CD_3CN; [c] TPSSh/SARC-ZORA-TZVP; [d] B3LYP/SARC-ZORA-TZVP; [e] axial triflate is not coordinated; [f] one of the pyridine rings is not coordinated.

^{89}Y NMR Spectroscopy

In continuation of our previous SP ligand system,[4] we conducted ^{89}Y NMR measurements to assess the varying donor abilities of the different ligands. The signals were consistently obtained using a robust and reproducible indirect-detection two-dimensional method, specifically the ^{1}H, ^{89}Y HMBC NMR experiments as previously described.[4,18] Across all the 2D maps, the ^{89}Y signal displayed scalar interaction not only with the imine proton but also with both methylene groups in the ligand backbone, attributed to the larger ^3J coupling between these protons and the spin 1/2 yttrium nucleus, verifying further the coordination of the yttrium metal with the nitrogen at the apical position. The ^{89}Y chemical shifts ranged from 45.3 to 154.7 ppm as is illustrated in Table 4.

Lätsch *et al.* have already shown that the yttrium signal appears at lower chemical shifts when strongly donating atoms surround the metallic nucleus.[19] This trend remains consistent with increasing coordination numbers, further emphasizing that a stronger donating ligand system or increased coordination with triflates leads to lower chemical shifts. The experimental and computational determination of these chemical shifts is displayed in Table 4. Figure 4a additionally illustrates the correlation between the degree of ion pairing and the yttrium chemical shift. As previously mentioned, this representation reveals a linear negative slope, indicating an inverse relationship between the ion-pairing degree and the chemical shift.

The lowest frequency signal, observed at δ_{89Y} = 45.3 ppm for the **Y(^{5Me}pz$_3$tren)** complex, correlates in Figure 4a with the highest degree of ion-pairing (D_C/D_A = 0.84) of the entire yttrium complex series. Similarly, the **Y(py$_3$tren)** complex exhibits a low chemical shift of δ_{89Y} 75.8 ppm, which again aligns with a significant extent of ion-pairing (D_C/D_A = 0.78). In the solid-state, crystal structures of **Ce(^{Me}im$_3$tren)** and **La(^{Me}im$_3$tren)** illustrate the coordination of all triflate anions to the metal center, and therefore a similar coordination pattern is expected for **Y(^{Me}im$_3$tren)**, wherein a low ^{89}Y chemical shift of δ_{89Y} 78.9 ppm is anticipated, indicative of a high degree of ion pairing (D_C/D_A = 0.75).

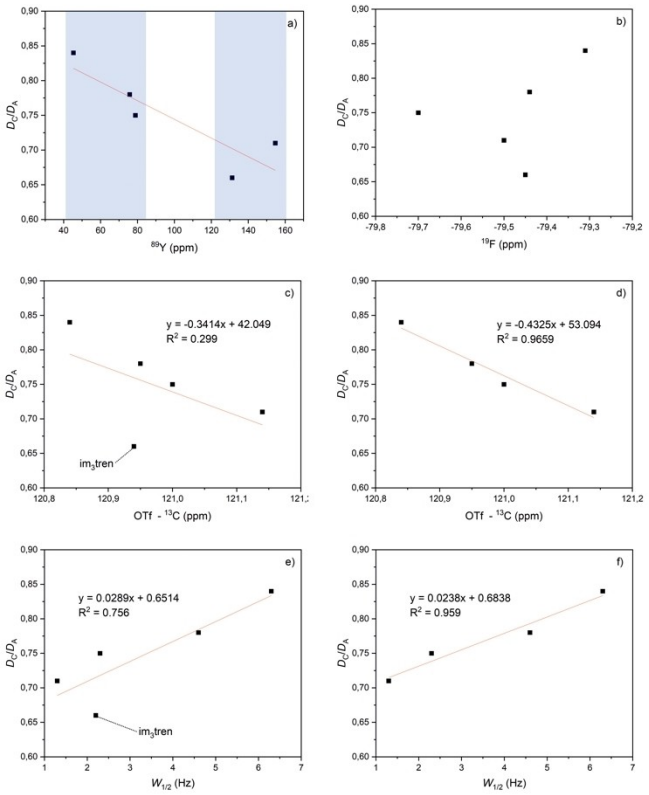

Figure 4. Ion pairing degree (D_C/D_A) as a function of a) ^{89}Y chemical shift, b) ^{19}F triflate chemical shift, c) ^{13}C triflate chemical shift, and e) ^{19}F full width at half maximum ($W_{1/2}$) of the triflate signal. Linear correlations excluding the data from **Y(im$_3$tren)** are given in d) and f).

Conversely, high-frequency signals located at δ_{89Y} 131.3 and 154.7 ppm are observed for **Y(im$_3$tren)** and **Y((^{4Me})im$_3$tren)**, respectively, corresponding to low values of ion-pairing (Figure 4a). In these complexes, the third triflate counter ion appears more dissociated than in others, aligning with the experimental data. For **Y((^{4Me})im$_3$tren)**, this behavior may relate to the observed high steric hindrance evident in the steric maps given in Figure 2. Regarding **Y(im$_3$tren)**, the highest chemical shift aligns with a structural comparison to **La(im$_3$tren)**, wherein an acetonitrile molecule coordinates to the metal center in the axial position. This change in the coordination sphere alters the metal coordination abilities with the triflate, consequently reducing the ion-pairing. Figure 4a visually depicts this linear correlation, delineating two distinct regions that have been shaded.

The correlation between ion pairing and several other structural features was examined, including the ^{19}F triflate signal and its full width at half maximum ($W_{1/2}$), as well as the ^{13}C chemical shift of the averaged triflate. Our premise was that if triflates are main players in the coordination, spectral features might also be affected by the degree of ion pairing.

Figure 4b–f illustrates these correlations. Notably, in Figure 4d and f, the data from **Y(im$_3$tren)** were excluded, resulting in a significant improvement in linearity. Unfortunately, the ^{19}F NMR chemical shift (Figure 4b) did not exhibit an evident correlation. However, a clear correlation emerged when utilizing the $W_{1/2}$ of the ^{19}F signal and the chemical shift of the averaged triflates. In Figure 4d, the trend mirrors that observed with the yttrium chemical shift, where a higher chemical shift corresponds to a lower degree of ion-pairing. Conversely, in Figure 4f, the trend is inverted, indicating that a higher linewidth corresponds to a higher degree of ion-pairing.

To corroborate the experimental chemical shifts and to elucidate the number of coordinated triflate groups, DFT calculations were also conducted. Theoretical chemical shifts of yttrium complexes with three coordinated triflate ions, as well as cationic yttrium complexes with one uncoordinated triflate group have been calculated (**Y(het)** and **[Y(het)-X]$^+$**, in Table 4). The calculated results are comparable with the experimental ones. For **Y(py$_3$tren)**, the experimental ^{89}Y shift is in good correlation with the theoretical one obtained for the neutral complexes with three coordinated triflate groups. These results support the higher ion pairing obtained by diffusion NMR. For **Y(im$_3$tren)** and **Y((^{Me})im$_3$tren)**, the experimental ^{89}Y chemical shifts fit better with the calculated ones for the cationic complexes **[Y(het)-X]$^+$** with a non-coordinated triflate anion. **Y(im$_3$tren)** and **Y((^{Me})im$_3$tren)** display lower ion pairing as **Y(py$_3$tren)** and the results are coherent. The calculations done for **Y((^{4Me})im$_3$tren)** and **Y((^{5Me})pz$_3$tren)** are differing from the other complexes. Indeed, in the case of the neutral complexes **Y(het$_3$tren)**, the calculations assume that the axial triflate group is not coordinating, leaving the axial position free. For **Y((^{4Me})im$_3$tren)** the experimental results fit with the theoretical ones for **Y(het$_3$tren)**, which support the low ion pairing in solution. For **Y((^{5Me})pz$_3$tren)**, the experimental chemical shift is shifted to high frequencies comparing to the theoretical one for the neutral complex **Y(het$_3$tren)**, which attests to a higher ion pairing in solution in reality. Compared to the results obtained in our previous study for the SP-complexes, the experimental ^{89}Y shifts of **Y(het$_3$tren)** are shifted to higher frequencies and therefore the third triflate might be more solvated. This agrees well with XRD observations. For the SP-complexes all triflate groups were coordinated to the yttrium metal center in the solid state, which is not the case for the tren-complexes. The tren-ligands scaffold appears to be more sterically bulky compared to the SP-ligands. Moreover, as mentioned earlier, the coordination of the apical nitrogen N_{tren} possibly hinders the binding of the third axial triflate anion.

DFT Calculations

Computational studies on the ligand systems have been performed to quantify the donor ability. We computed (TPSSh/QZVPP/D3-BJ) the proton affinities (PA) and the energies of the donor orbital (E_{orb}) of one isolated *N*-donor ligand entity. The results are given in Table 5 and Figure 5.

For none of the ligands the HOMO is the corresponding donor orbital. The calculated PA are varying between 977–1023 kJ/mol, the energy of the donor orbitals shows values between −6.55 to −6.13 eV. Taking the proton affinities into account, the following order of donor strengths results:

^{Me}im$_3$tren > ^{4Me}im$_3$tren > py$_3$tren > im$_3$tren > ^{5Me}pz$_3$tren

Table 5. Computed (TPSSh/QZVPP/D3BJ) donor orbital energies (E_{orb}) and proton affinities (PA).

	PA/kJ/mol	E_{orb}/eV	donor orbital
im$_3$tren	1005	−6.55	HOMO-2
^{Me}im$_3$tren	1023	−6.44	HOMO-2
^{4Me}im$_3$tren	1017	−6.13	HOMO-2
^{5Me}pz$_3$tren	977	−6.26	HOMO-2
py$_3$tren	1011	−6.39	HOMO-1

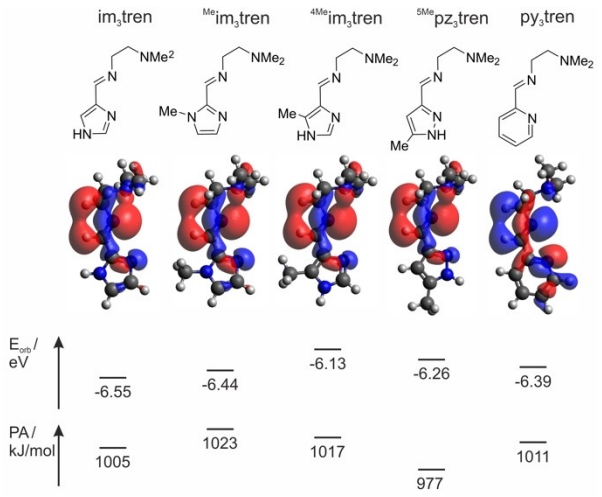

Figure 5. Plotted (iso = 0.02) donor orbitals ([**im$_3$tren**]: HOMO-2; [**^{Me}im$_3$tren**]: HOMO-2; [**^{4Me}im$_3$tren**]: HOMO-2; [**^{5Me}pz$_3$tren**]: HOMO-2; [**py$_3$tren**]: HOMO–1) energies of the donor orbitals and proton affinity of the isolated ligand arms.

As expected, this represents the same trend as obtained with the SP-ligands.[4] Following the energies of the corresponding donor orbitals (assuming the highest energy correlates with the strongest donor abilities), the order is:

^{4Me}**im$_3$tren** > ^{5Me}**pz$_3$tren** > **py$_3$tren** > ^{Me}**im$_3$tren** > **im$_3$tren**,

which is not correlating with the results obtained for the SP-ligands. Indeed, ^{4Me}**im$_3$tren** and ^{5Me}**pz$_3$tren** display higher E_{orb} as their SP-analogues and are, based on these results, better donating ligands than **py$_3$tren**. In our previous study, **py$_3$tren** was the strongest donor of the series concerning the donor orbital energy. As for the PA and E_{orb} studies of the SP-ligands, ^{4Me}**im$_3$tren** is consistently one of the strongest donors.

Electrochemistry

To determine the donating character of the ligands electrochemical studies were performed. Indeed, the oxidation potential of Ce^{III}/Ce^{IV} redox couple enables the quantification of the donor strength of the ligands. Low oxidation potentials usually correlate with high donor abilities of the ligand. The experimental oxidation potentials are reported in Table 6. All complexes display irreversible redox processes, except for **Ce(im$_3$tren)**, for which a quasi-reversible redox process is observed (see Supporting Information, Section S1, Figure S1a). Because of the weak intensity of the **Ce(im$_3$tren)** reduction peak, it could not be excluded that it corresponds to a solvent impurity and the values are written in grey in Table 6. In this study, the focus is on the oxidation potentials and the reduction peak could be ignored. As for the SP-ligands and for the reported cerium complexes with polydentate *N*-donor ligands, the intensity of the oxidation wave is weaker than the intensity of the reduction peak.[20] From the measured oxidation potentials the following trend is obtained for donor strength:

im$_3$tren > ^{4Me}**im$_3$tren** > ^{Me}**im$_3$tren** > **py$_3$tren** > ^{5Me}**pz$_3$tren**,

in which **im$_3$tren** is the ligand with the highest donating character.

Table 6. Measured first oxidation and reduction potentials of the synthesized cerium complexes in acetonitrile vs Fc/Fc^+ (internal standard Fc/Fc^+; conditions: Pt/[NBu_4][PF_6]/Ag; v = 100 (first values) and 250 mV/s (second values).

Compound	E_{ox}/V	I_{pa}/μA	E_{red}/V	I_{pc}/μA	E_{ox}–E_{red}/V
Ce(im$_3$tren)	−1.04	0.32	−1.52	0.57	0.48
	−1.01	0.44	−1.43	0.80	0.42
Ce(^{Me}im$_3$tren)	0.52	0.02	−1.16	0.05	1.68
	0.56	0.02	−1.16	0.11	1.74
Ce(^{4Me}im$_3$tren)	−0.75	0.35	−1.52	0.78	0.77
	−0.75	0.49	−1.70	0.46	0.95
Ce(^{5Me}pz$_3$tren)	1.95	0.94	−1.82	0.73	3.77
	1.92	1.50	−1.90	1.54	3.82
Ce(py$_3$tren)	–	–	−1.55	4.59	–
	1.39	0.61	−1.63	7.02	3.02
Ce(terpy)$_2$	1.71	0.22	−1.01	0.10	2.72
	1.71	0.76	−1.10	0.31	2.81

Because of the weak intensity of the experimental oxidation potentials, DFT calculations have been performed to confirm the experimental study (Table 7 and Table 8). Considering the solid-state crystal structure of the different complexes, calculations with three coordinated triflate groups but also with only two coordinated triflate counter ions with additional acetonitrile molecule, have been performed.

In Table 8, the results of the complexes with two coordinated triflate counter ions and one coordinating acetonitrile molecule are shown. The following trend is obtained:

^{4Me}**im$_3$tren** > ^{Me}**im$_3$tren** > **im$_3$tren** > **py$_3$tren** > ^{5Me}**pz$_3$tren**

where ^{4Me}**im$_3$tren** is the ligand with the highest donor strength. The trends obtained do not correspond exactly to the trends of the SP-ligands, but ^{4Me}**im$_3$tren** is the ligand that consistently has one of the highest donor characters in both systems. Another similarity is that ^{5Me}**pz$_3$tren** and **py$_3$tren** are the ligands with the lowest donating strength in both studies. In the previous NMR study, ^{5Me}**pz$_3$tren** and **py$_3$tren** display the highest ion pairing and ^{4Me}**im$_3$tren** the lowest. The donor strength of the ligand could influence the degree of ion pairing. Indeed, it seems that the higher the donor strength the more the lanthanide ion is encapsulated in the ligand system.

All the investigated cerium(III) complexes are paramagnetic. To investigate where the single electron is localized in the structure of the complexes, the spin density was calculated on the TPSS/TZVP level of theory including D3BJ dispersion correction.[21] The calculations display a localization of the spin

Table 7. Neutral Ce complexes with three OTf ligands. Computed (TPSS/TZVP/D3BJ), ionization energies (gas phase), HOMO energies (gas phase) and $E_{1/2}$ vs. Fc/Fc^+ including solvent effects (MeCN).

Complex	E_{Ion} (gas)	E_{HOMO}/eV (gas)	$E_{1/2}$/V	$E_{1/2}$/V (MeCN)
Ce(im$_3$tren)	584.12	−3.70	4.78	0.12
Ce(^{Me}im$_3$tren)	575.36	−3.54	4.72	0.06
Ce(^{4Me}im$_3$tren)	566.55	−3.33	4.59	−0.07
Ce(^{5Me}pz$_3$tren)	596.85	−3.72	4.78	0.12
Ce(py$_3$tren)	593.58	−3.88	4.87	0.21

Table 8. Cationic Ce complexes with two OTf^- and one MeCN ligands. Computed (TPSS/TZVP/D3BJ) energies including the thermal correction, ionization energies (gas phase), HOMO energies (gas phase) and $E_{1/2}$ vs Fc including solvent effects (MeCN).

Complex	E_{Ion} (gas)	E_{HOMO}/eV (gas)	$E_{1/2}$/V	$E_{1/2}$/V (MeCN)
[Ce(im$_3$tren)-X]$^+$	836.77	−6.08	4.80	0.14
[Ce(^{Me}im$_3$tren)-X]$^+$	819.40	−5.99	4.79	0.13
[Ce(^{4Me}im$_3$tren)-X]$^+$	792.54	−5.75	4.62	−0.04
[Ce(^{5Me}pz$_3$tren)-X]$^{+a}$	859.04	−6.20	5.00	0.34
[Ce(py$_3$tren)-X]$^+$	840.69	−6.34	4.90	0.24

[a] The MeCN ligand is not coordinated to the cerium atom.

density at the cerium atom, which supports the hypothesis that the first oxidation occurs at the Ce^{3+} center. A representation of the localization of the spin density is shown in Section S6, Figure S92 of the Supporting Information.

UV-vis Spectroscopy

To obtain additional information about the donating ability of the ligands, we measured the UV-vis spectra of the cerium complexes in MeCN at 298 K (Figure 6a). Additionally, we performed computational investigations using TD-DFT at the TPSSh/TZVP level of theory, with incorporated solvent effects CPCM(MeCN) (Figure 6b and c). The measured absorption maxima for the different cerium complexes are reported in Table 9 and two to three absorption maxima are detected for the **Ce(het$_3$tren)** series (λ_1, λ_2 and λ_3). The lowest absorption maximum is observed for **Ce(im$_3$tren)** ($\lambda_1 = 218.6$ nm) followed by **Ce(^{4Me}im$_3$tren)** ($\lambda_1 = 225.0$ nm). The higher absorption maximum is observed for **Ce(^{4Me}im$_3$tren)** ($\lambda_3 = 331.2$ nm) followed by **Ce(^{5Me}pz$_3$tren)** ($\lambda_2 = 322.4$ nm). It is to note, that **Ce(^{5Me}pz$_3$tren)** display one of the highest absorption maxima even though it just displays two (λ_1 and λ_2). For the absorption maxima λ_1 and λ_2, the same trend is observed:

λ(**im$_3$tren**) < λ(**^{4Me}im$_3$tren**) < λ(**py$_3$tren**) < λ(**^{Me}im$_3$tren**) < λ(**^{5Me}pz$_3$tren**).

Once more, the experimental UV–vis spectra were substantiated with theoretical studies. The computed absorption maxima are reported in Table 10. As for the ^{89}Y NMR chemical shifts and for the electrochemical study, calculations have been done for three coordinating triflate groups and for one non coordinating triflate anion (**Ce(het$_3$tren)** and **[Ce(Het$_3$tren)-OTf]$^+$**). The trend obtained for both complexes' species are differing. Although the trend obtained for the cationic complexes is more fitting with the measured absorption maxima. The trend obtained from the absorption maxima of the **[Ce(het$_3$tren)-OTf]$^+$** series is the following:

λ(**im$_3$tren**) < λ(**^{4Me}im$_3$tren**) < λ(**^{Me}im$_3$tren**) < λ(**py$_3$tren**) < λ(**^{5Me}pz$_3$tren**).

This trend is identical to the one obtained by cyclic voltammetry.

Selectivity Studies

To investigate the selectivity of the ligands toward the different Ln(OTf)$_3$ (Ln=Y, La, Sm, Lu), selectivity studies were carried out by mixing one equivalent of ligand with one equivalent of each lanthanide precursor. The solvents varied from methanol to THF depending on the solvent used for complexation. All experiments carried out in THF were repeated in acetonitrile, because of different solubility of the complexes in THF. The obtained results are graphically shown in Figure 7. As for the SP-ligands from our previous study, the complexation with Lu(OTf)$_3$ is favoured, the small ionic radius of lutetium facilitates the complexation. For all tren-ligands, complexation with Sm(OTf)$_3$ is observed, too. Besides **py$_3$tren**, all ligands are complexing

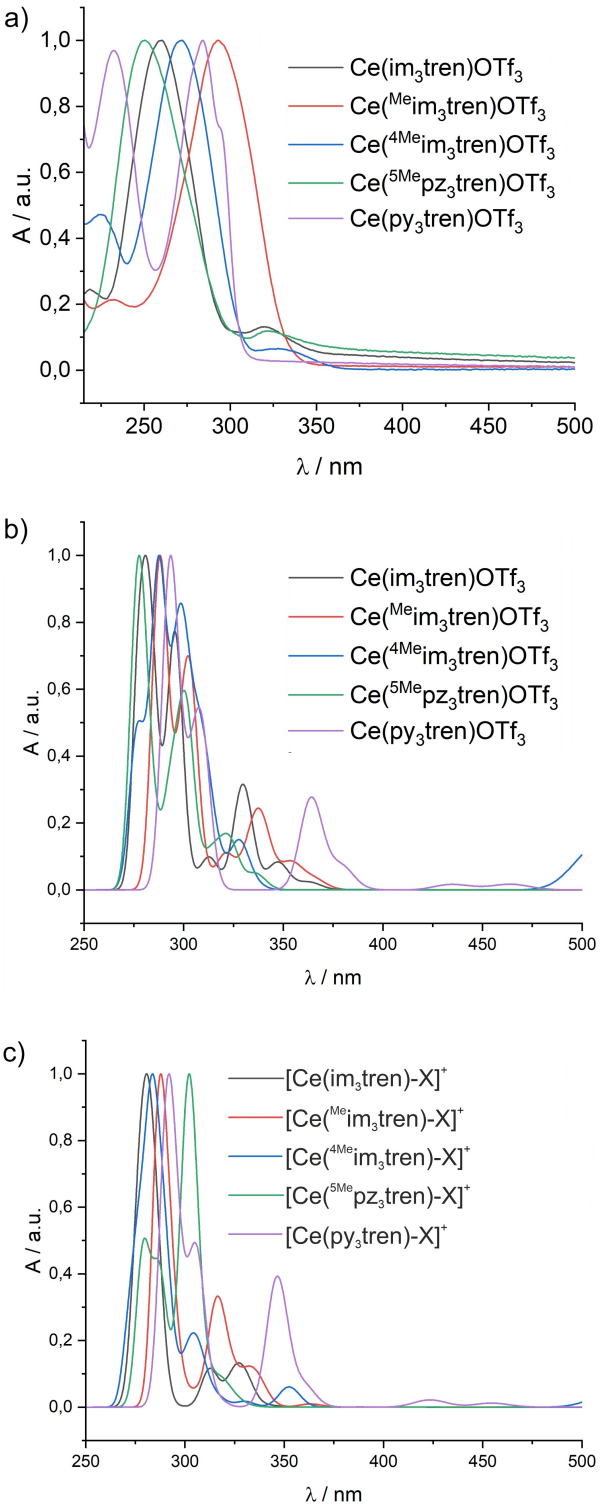

Figure 6. (a) Absorption spectra of **Ce(im$_3$tren)**, **Ce(^{Me}im$_3$tren)**, **Ce(^{4Me}im$_3$tren)**, **Ce(^{5Me}pz$_3$tren)** and **Ce(py$_3$tren)** in MeCN at 298 K; Computed UV-vis absorption spectra in MeCN with (b) three coordinated triflate counter ions and (c) two coordinated triflate counter ions.

Y(OTf)$_3$ and **py$_3$tren** seems to be the most selective ligand with up to 88.5% of complexation with Lu(OTf)$_3$ in acetonitrile. Complexation with La(OTf)$_3$ is observed for **^{4Me}im$_3$tren** in

Table 9. Experimental UV-Vis absorption maxima.

Complex	λ_1/nm	λ_2/nm	λ_3/nm
Ce(im$_3$tren)	218.6	260.4	320.0
Ce(^{Me}im$_3$tren)	232.6	293.6	
Ce(^{4Me}im$_3$tren)	225.0	272.0	331.2
Ce(^{5Me}pz$_3$tren)	250.6	322.4	
Ce(py$_3$tren)	232.4	284.0	295.2

Table 10. TD-DFT (TPSSh/TZVP, including solvent effects (MeCN)) calculations of Ce complexes with two (top) and three (bottom) OTf ligands.

Complex	$\lambda_{max/calc.}$/ nm	$E_{max/calc.}$/ eV	Transition
Ce(im$_3$tren)	288	4.30	M→L
Ce(^{Me}im$_3$tren)	289	4.30	M→L; L→L (L→M)[a]
Ce(^{4Me}im$_3$tren)	288	4.31	M→L and L→L
Ce(^{5Me}pz$_3$tren)	278	4.46	M→L and L→L
Ce(py$_3$tren)	294	4.22	L→L (M→L)[a]
[Ce(im$_3$tren)-X]$^+$	282	4.40	M→L; L→L (L→M)[a]
[Ce(^{Me}im$_3$tren)-X]$^+$	287	4,33	M→L; L→L (L→M)[a]
[Ce(^{4Me}im$_3$tren)-X]$^+$	284	4.36	M→L and L→L
[Ce(^{5Me}pz$_3$tren)-X]$^+$[b]	302	4.10	M→L; L→L (L→M)[a]
[Ce(py$_3$tren)-X]$^+$	294	4.22	L→L (M→L)[a]

[a] Small contribution. [b] The MeCN ligand is not coordinated to the cerium atom.

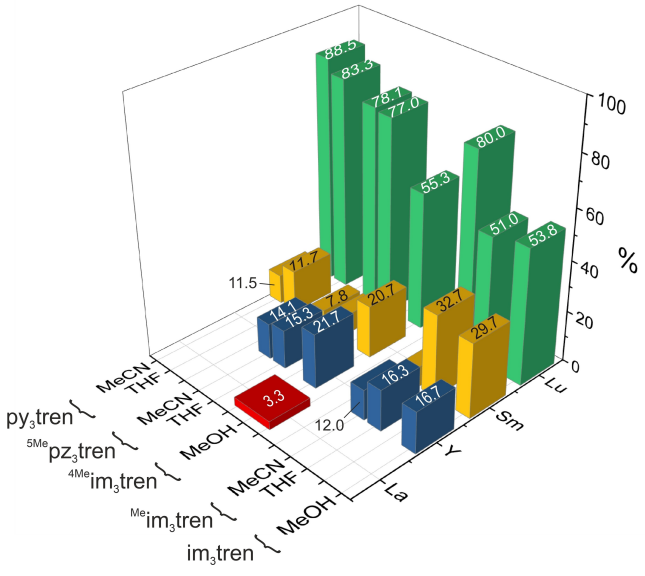

Figure 7. Results of the selectivity studies of each ligand with the lanthanide precursors. Reaction solutions were stirred overnight at 298 K in MeOH, MeCN or THF.

methanol thereby **^{4Me}im$_3$tren** seems to be the least selective ligand. To investigate the coordination preference of the lanthanides between the tren- and the SP-ligands, competition studies have been performed. For that, a tren-ligand and its corresponding SP-analogue (for example **im$_3$tren** and **SP(im)**) were mixed with Lu(OTf)$_3$ and stirred overnight. In all cases, no complexation with the SP-ligands was observed. Lu(OTf)$_3$ is complexing to 100% with the corresponding tren-ligand. The increased flexibility made the coordination with lutetium faster and the selectivity for small ionic radii is enhanced.

Conclusion

Several rare-earth-metal complexes, employing ligands consistent with the CHON principle have been synthesized and characterized both in the solid state and in solution. The structure and solution behavior of these complexes have been investigated using methodologies already detailed in our previous publication. Notably, the tren-complexes display lower ion pairing compared to their SP-analogues, a phenomenon supported by XRD analysis, structural parameters, and ^{89}Y NMR studies. The donating character of the involved ligands has been extensively explored through various spectroscopic and electrochemical techniques, corroborated by computational studies. The **im**- and **^{4Me}im**-based ligands demonstrate the highest donating strength, while **^{5Me}pz$_3$tren** and **py$_3$tren** exhibit the lowest. Importantly, the donating character appears to influence ion pairing in solution. Furthermore, the tren-ligands exhibit a greater propensity to complex lutetium, consistent with our previous findings. However, competition studies between the tren- and SP-ligands revealed that Lu(OTf)$_3$ exclusively complexes with the tren-based ligands. This observation suggests that in addition to adhering to the CHON principle, the higher flexibility of the tren-ligands provides an enhanced ability to coordinate with lutetium ions. This research aims to optimize these processes and to contribute to the development of sustainable solutions for nuclear waste management.

Experimental Section

Computational details: All calculations have been performed with the ORCA 5.0.3 program.[22] Further details are given in the Supporting information, Section S6.[25–38]

General methods: All operations were carried out under dry argon using standard Schlenk and glovebox techniques. THF was freshly distilled under argon from sodium/benzophenone, diethyl ether and diisopropyl ether from sodium–potassium alloy/benzophenone and acetonitrile from CaH_2 prior to use. CD_3CN was vacuum transferred from CaH_2 into thoroughly dried glassware equipped with Young Teflon valves. All chemicals were purchased from Aldrich or abcr and used as received.

IR spectra were measured on a Bruker Alpha spectrometer using the attenuated reflection technique (ATR) and the data are quoted in wavelength numbers [cm^{-1}]. The intensity of the absorption band is indicated as vw (very weak), w (weak), m (medium), s

(strong), vs. (very strong), and br (broad). Melting points were measured with a Thermo Fischer melting point apparatus and are not corrected. A Perkin–Elmer Lambda 9 UV/Vis spectrophotometer was used for recording absorption spectra at room temperature. Cyclic voltammetry measurements were performed with Gamry or Metrohm potentiostats and an electrochemical cell within a glovebox. We used a freshly polished Pt disc working electrode, a Pt wire as counter electrode, and a Ag wire as (pseudo) reference electrode {[nBu$_4$N][PF$_6$] (0.5 M) as electrolyte}. Potentials were calibrated against the Fc/Fc$^+$ couple (internal standard). NMR spectra were recorded on Bruker AV 300, AV 400 and Avance Neo 400 spectrometers in dry degassed deuterated solvents. ^{1}H, ^{13}C{^{1}H} chemical shifts are reported against TMS and ^{31}P{^{1}H} against H_3PO_4, $CFCl_3$ for ^{19}F, NH_3 for ^{15}N and Y(NO$_3$)$_3$ for ^{89}Y. Coupling constants (J) are given in Hertz as positive values, regardless of their real individual signs. The multiplicity of the signals is indicated as s, d or m for singlet, doublet or multiplet respectively. The assignments were confirmed, as necessary, with the use of 2D NMR correlation experiments. Subscript indexes such as py, im or pz are given for entities belonging to the pyridyl, imine, or pyrazolyl subunits of the ligand, respectively. PGSE NMR diffusion measurements were carried out using the stimulated echo pulse sequence.[23] A rectangular shape was used for the gradient pulses and their strength varied automatically in the course of the experiments. The D values were determined from the slope of the regression line ln(I/I$_0$) versus G^2, according to Equation (1). I/I$_0$ = observed spin echo intensity/intensity without gradients, G = gradient strength, Δ = delay between the midpoints of the gradients, D = diffusion coefficient, δ = gradient length.

$$ln\left(\frac{I}{I_0}\right) = -(\gamma\delta)^2 G^2\left(\Delta - \frac{\delta}{3}\right)D \quad (1)$$

The measurements were carried out without spinning. Gradient calibration was carried out by means of a diffusion measurement of HDO in D_2O (D(HDO) = 1.902×10^{-9} m^2 s^{-1}).[24] The experimental error in D values was estimated to be smaller than ±2% (3 standard deviations). All the data leading to the reported D values afforded lines whose correlation coefficients were above 0.999. The gradient strength was incremented in 4–8% steps from 2–10% to 98% so that, depending on the signal to noise ratio, 12–25 points could be used for regression analysis.

Materials and Reagents

im$_3$tren, **^{Me}im$_3$tren**, **^{4Me}im$_3$tren** and **py$_3$tren** were prepared according to literature methods.[7–10] Note that for the complexes described in this paper, no elemental analyses could be obtained due to the high fluorine content of the sample (triflate counter ion).

Ligand: **^{5Me}pz$_3$tren**: tren (0.75 mL, 5 mmol) and MgSO$_4$ were suspended in methanol (50 mL). 5-methyl-1*H*-pyrazol-3-carboxaldehyde was added, and the mixture was refluxed overnight. After cooling down to room temperature the mixture was filtered through celite, and the obtained solution was evaporated to dryness with a rotary evaporator. The product was obtained as orange solid (710.5 mg, 1.68 mmol, 55%). M.p.: >175 °C decomp. ^{1}H NMR (400.1 MHz, 298.8 K, CD$_3$CN) δ = 8.18 (s, 3H, N=C*H*), 6.41 (s, 3H, *H*-pz), 3.69–3.63 (m, 6H, CH_2-2), 2.90 (t, J = 6.6 Hz, 6H, CH_2-1), 2.29 (s, 9H, *Me*-pz). ppm. ^{13}C{^{1}H} NMR (75.48 MHz, 298.8 K, CD$_3$CN):δ = 158.15 (s, N=*C*H), 104.13 (s, H-*pz*), 60.51 (s, *C*H$_2$-2), 56.24 (s, *C*H$_2$-1), 25.25 (s), 10.97(s, *Me*-pz) ppm. FT-IR (solid, ATR): 3755 (vw), 2434 (vw), 2259 (w), 2244 (w), 2226 (vw), 2215 (vw), 2182 (w), 2173 (vw), 2161 (w), 2134 (m), 2118 (w), 2084 (w), 2071 (w), 2062 (w), 2050 (w), 2032 (m), 2022 (w), 2003 (w), 1995 (w), 1982 (w), 1972 (w), 1959 (w), 1935 (w), 1917 (vw), 1891 (vw), 1652 (vw), 797 (w), 788 (w), 764 (vw), 742 (vw), 685 (vw), 645 (vw), 617 (vw), 599 (w), 590 (vw), 565 (w), 557 (vw), 547 (w), 536 (w), 528 (vw), 510 (w), 491 (w), 482 (m), 457 (s), 449 (s), 431 (vs), 407 (vs), 401 (vs), 392 (m), 383 (vs) cm^{-1}.

Complexes: Ligand (**het$_3$tren**) and Ln(OTf)$_3$ were dissolved in stoichiometric quantities in THF or methanol and stirred overnight at room temperature. The forming precipitate was filtered and washed two times with THF. The resulting solid was dissolved in acetonitrile and layered with diisopropyl ether or diethyl ether. (For the reactions in methanol where no precipitate forms: the clear solution was evaporated to dryness and the obtained solid dissolved in acetonitrile and overlayed with ether to obtain pure product). Used solvents and isolated yields are displayed in Table 11.

Y(im$_3$tren): M.p.: >100 °C decomp. ^{1}H NMR (400.1 MHz, 298.8 K, CD$_3$CN) δ = 11.16 (s, 3H, N*H*), 8.41–8.34 (m, 3H, N=C*H*), 7.71 (s, 3H), 7.69 (d, J = 1.1 Hz, 3H), 4.02–3.88 (m, 6H, CH_2-2), 3.22 (t, J = 6.2 Hz, 6H, CH_2-1) ppm. ^{13}C{^{1}H} NMR (75.48 MHz, 298.8 K, CD$_3$CN): δ = 161.24 (s, N=CH), 140.22 (s), 138.60 (s), 124.06 (s), 120.94 (d, $^1J_{CF}$ = 319.2 Hz), 60.08 (s, *C*H$_2$-1), 56.87 (s, *C*H$_2$-2) ppm. ^{19}F NMR (282.40 MHz, 298.8 K, CD$_3$CN): δ = −79.5 (s) ppm. ^{89}Y NMR (19.61 MHz, 298.8 K, CD$_3$CN): δ = 131.3 ppm. FT-IR (solid, ATR): see the Supporting Information.

La(im$_3$tren): M.p.: 160–170 °C. ^{1}H NMR (400.1 MHz, 298.8 K, CD$_3$CN): δ = 8.32–8.26 (m, 3H, N=C*H*), 7.76 (s, 3H), 7.56 (d, J = 1.1 Hz, 3H), 3.95–3.72 (m, 6H, CH_2-2), 3.09–3.00 (m, 6H, CH_2-1) ppm. ^{13}C{^{1}H} NMR (75.48 MHz, 298.8 K, CD$_3$CN): δ = 158.89 (s, N=CH), 140.03 (s), 138.93

Table 11. Reaction solvent and isolated yields of the complexes.

Compound	Reaction solvent	Isolated yield [%]
Y(im$_3$tren)	MeOH	75
La(im$_3$tren)	MeOH	58
Ce(im$_3$tren)	MeOH	47
Sm(im$_3$tren)	MeOH	45
Lu(im$_3$tren)	MeOH	42
Y(^{Me}im$_3$tren)	THF	64
La(^{Me}im$_3$tren)	THF	68
Ce(^{Me}im$_3$tren)	THF	63
Sm(^{Me}im$_3$tren)	THF	65
Lu(^{Me}im$_3$tren)	THF	67
Y(^{4Me}im$_3$tren)	MeOH	67
La(^{4Me}im$_3$tren)	MeOH	33
Ce(^{4Me}im$_3$tren)	MeOH	46
Sm(^{4Me}im$_3$tren)	MeOH	38
Lu(^{4Me}im$_3$tren)	MeOH	56
Y(^{5Me}pz$_3$tren)	THF	64
La(^{5Me}pz$_3$tren)	THF	27
Ce(^{5Me}pz$_3$tren)	THF	40
Sm(^{5Me}pz$_3$tren)	THF	32
Lu(^{5Me}pz$_3$tren)	THF	62
Y(py$_3$tren)	THF	5
La(py$_3$tren)	THF	43
Ce(py$_3$tren)	THF	57
Sm(py$_3$tren)	THF	5
Lu(py$_3$tren)	THF	67

(s), 123.15 (s), 61.46 (s, CH_2-1), 59.21 (s, CH_2-2) ppm. ^{19}F NMR (282.40 MHz, 298.8 K, CD_3CN): δ = −79.5 (s) ppm. FT-IR (solid, ATR): see the Supporting Information.

Ce(im$_3$tren): M.p.: >165 °C decomp. ^{1}H NMR (400.1 MHz, 298.8 K, CD_3CN) δ = 18.29 (s, 3H), 11.29 (s, 3H), 4.68 (s, 3H), 3.79 (s, 6H), −4.10 (s, 6H) ppm. $^{13}C\{^1H\}$ NMR (75.48 MHz, 298.8 K, CD_3CN): δ = 168.22 (s), 149.13 (s), 146.31 (s), 131.66 (s), 52.90 (s), 45.20 (s) ppm. ^{19}F NMR (282.40 MHz, 298.8 K, CD_3CN): δ = −79.7 (s) ppm. Because of paramagnetism, too little information could be obtained from the 2D spectra, and no assignment of the different signals was possible. FT-IR (solid, ATR): see the Supporting Information.

Sm(im$_3$tren): M.p.: >210 °C decomp. ^{1}H NMR (400.1 MHz, 298.8 K, CD_3CN) δ = 8.71 (s, 3H, N=C*H*), 8.07 (s, 3 H), 6.59 (s, 3 H), 3.87 (s, 6H, CH_2-2), 1.37 (t, *J* = 6.1 Hz, 6H, CH_2-1) ppm. $^{13}C\{^1H\}$ NMR (75.48 MHz, 298.8 K, CD_3CN): δ = 165.11 (s, N=*C*H), 143.21 (s), 138.26 (s), 123.95 (s), 58.70 (s, CH_2-1), 58.33 (s, CH_2-2) ppm. ^{19}F NMR (282.40 MHz, 298.8 K, CD_3CN): δ = −79.6 (s) ppm. FT-IR (solid, ATR): see the Supporting Information.

Lu(im$_3$tren): M.p.: >250 °C decomp. ^{1}H NMR (400.1 MHz, 298.8 K, CD_3CN) δ = 10.34 (s, 3H, N*H*), 8.49 (s, 3 H, N=C*H*), 7.72 (d, *J* = 0.9 Hz, 3H), 7.62 (d, *J* = 43.0 Hz, 3H), 4.03–3.89 (m, 6H, CH_2-2), 3.23 (t, *J* = 6.1 Hz, 6 H, CH_2-1) ppm. $^{13}C\{^1H\}$ NMR (75.48 MHz, 298.8 K, CD_3CN): δ = 162.21 (s, N=*C*H), 141.15 (s), 138.71 (s), 124.34 (s), 60.36 (s, CH_2-1), 57.02 (s, CH_2-2) ppm. ^{19}F NMR (282.40 MHz, 298.8 K, CD_3CN): δ = −79.5 (s) ppm. FT-IR (solid, ATR): see the Supporting Information.

Y(^{Me}im$_3$tren): M.p.: >210 °C decomp. ^{1}H NMR (400.1 MHz, 298.8 K, CD_3CN): δ = 8.47 (qd, *J* = 1.7, 0.6 Hz, 3H, N=C*H*), 7.27 (d, *J* = 1.4 Hz, 3H), 7.22–7.18 (m, 3H), 4.07 (td, *J* = 6.3, 1.8 Hz, 6H, CH_2-2), 3.82 (d, *J* = 4.4 Hz, 9H, N–*Me*), 3.28 (t, *J* = 6.4 Hz, 6H, CH_2-1) ppm. $^{13}C\{^1H\}$ NMR (75.48 MHz, 298.8 K, CD_3CN): δ = 154.58 (s, N=CH), 145.38 (s), 130.03 (s), 126.50 (s), 121.00 (d, $^1J_{CF}$ = 319.8 Hz), 59.51 (s, CH_2-1), 56.77 (s, CH_2-2), 34.48 (s, N–Me) ppm. ^{19}F NMR (282.40 MHz, 298.8 K, CD_3CN): δ = −79.7 (s) ppm. ^{89}Y NMR (19.61 MHz, 298.8 K, CD_3CN): δ = 78.9 ppm. FT-IR (solid, ATR): see the Supporting Information.

La(^{Me}im$_3$tren): M.p.: 190–205 °C. ^{1}H NMR (400.1 MHz, 298.8 K, CD_3CN): δ = 8.42 (s, 3H, N=C*H*), 7.19 (d, *J* = 1.4 Hz, 3H), 7.10 (s, 3H), 3.94 (td, *J* = 5.4, 1.3 Hz, 6H, CH_2-2), 3.82 (s, 9H, CH_3–N), 3.12–3.05 (m, 6 H, CH_2-1) ppm. $^{13}C\{^1H\}$ NMR (75.48 MHz, 298.8 K, CD_3CN): δ = 153.23 (s, N=*C*H), 145.17 (s), 130.66 (s), 125.53 (s), 61.37 (s, CH_2-1), 59.96 (s, CH_2-2), 34.24 (s, CH_3–N) ppm. ^{19}F NMR (282.40 MHz, 298.8 K, CD_3CN): δ = −79.7 (s) ppm. FT-IR (solid, ATR): see the Supporting Information.

Ce(^{Me}im$_3$tren): M.p.: >165 °C decomp. ^{1}H NMR (400.1 MHz, 298.8 K, CD_3CN) δ = 17.81 (s, 3H), 8.93 (s, 3H), 6.31 (s, 9H, N–CH_3) 4.31 (s, 3H), 3.46 (s, 6H), −3.71 (s, 6H) ppm. $^{13}C\{^1H\}$ NMR (75.48 MHz, 298.8 K, CD_3CN): δ = 156.68 (s, N=*C*H), 134.53 (s), 132.96 (s), 54.16 (s), 46.98 (s), 37.89 (s, N–CH_3) ppm. ^{19}F NMR (282.40 MHz, 298.8 K, CD_3CN): δ = −80.1 ppm. Because of paramagnetism, too little information could be obtained from the 2D spectra, and no assignments could be done. FT-IR (solid, ATR): see the Supporting Information.

Sm(^{Me}im$_3$tren): M.p.: >220 °C decomp. ^{1}H NMR (400.1 MHz, 298.8 K, CD_3CN) δ = 8.94 (s, 3 H, N=C*H*), 7.18 (d, *J* = 1.1 Hz, 3H), 5.92 (s, 3H), 4.21 (s, 9H, N–CH_3), 3.96 (t, *J* = 6.2 Hz, 6H, CH_2-2), 1.51 (t, *J* = 6.1 Hz, 6H, CH_2-1) ppm. $^{13}C\{^1H\}$ NMR (75.48 MHz, 298.8 K, CD_3CN): δ = 159.37 (s, N=CH), 149.65 (s), 129.38 (s), 125.70 (s), 58.59 (s, CH_2-1), 58.45 (s, CH_2-2), 34.96 (s, N–CH_3) ppm. ^{19}F NMR (282.40 MHz, 298.8 K, CD_3CN): δ = −79.8 ppm. FT-IR (solid, ATR): see the Supporting Information.

Lu(^{Me}im3tren): M.p.: >230 °C decomp. ^{1}H NMR (400.1 MHz, 298.8 K, CD_3CN): δ = 8.64 (q, *J* = 1.0 Hz, 3 H, N=C*H*), 7.33 (d, *J* = 1.3 Hz, 3 H), 6.88 (s, 3 H), 4.07 (td, *J* = 6.2, 1.6 Hz, 6H, CH_2-2), 3.87 (s, 9H, N–CH_3), 3.29 (t, *J* = 6.2 Hz, 6 H, CH_2-1) ppm. $^{13}C\{^1H\}$ NMR (75.48 MHz, 298.8 K, CD_3CN): δ = 157.01 (s, N=*C*H), 146.16 (s), 130.69 (s), 127.50 (s), 60.01 (s, CH_2-1), 57.37 (s, CH_2-2), 34.81 (s, N–CH_3) ppm. ^{19}F NMR (282.40 MHz, 298.8 K, CD_3CN): δ = −79.5 (s) ppm. FT-IR (solid, ATR): see the Supporting Information.

Y(^{4Me}im$_3$tren): M.p.: 145–165 °C. ^{1}H NMR (400.1 MHz, 298.8 K, CD_3CN): δ = 9.90 (s, 3H, N*H*), 8.41 (d, *J* = 10.1 Hz, 3 H, N=C*H*), 7.55 (s, 3H), 3.91 (t, *J* = 6.1 Hz, 6H, CH_2-2), 3.20 (t, *J* = 6.2 Hz, 6 H, CH_2-1), 2.38 (d, *J* = 3.8 Hz, 9H, *Me*-im) ppm. $^{13}C\{^1H\}$ NMR (75.48 MHz, 298.8 K, CD_3CN): δ = 160.70 (s, N=*C*H), 139.42 (s), 135.73 (s), 134.90 (s), 121.14 (d, $^1J_{CF}$ = 319.6 Hz), 60.26 (s, CH_2-1), 56.85 (s, CH_2-2), 9.58 (s, *Me*-im) ppm. ^{19}F NMR (282.40 MHz, 298.8 K, CD_3CN): δ = −79.5 (s) ppm. ^{89}Y NMR (19.61 MHz, 298.8 K, CD_3CN): δ = 154.7 ppm. FT-IR (solid, ATR): see the Supporting Information.

La(^{4Me}im$_3$tren): M.p.: 165–185 °C. ^{1}H NMR (400.1 MHz, 298.8 K, CD_3CN) δ = 8.30 (s, 3H, N=C*H*), 7.62 (s, 3H), 3.95–3.68 (m, 6H, CH_2-2), 3.11–2.98 (m, 6H, CH_2-1), 2.36 (d, *J* = 2.9 Hz, 9H, *Me*–im) ppm. $^{13}C\{^1H\}$ NMR (75.48 MHz, 298.8 K, CD_3CN): δ = 158.39 (s, N=*C*H), 138.79 (s), 135.02 (s), 134.15 (s), 61.05 (s, CH_2-1), 58.77 (s, CH_2-2), 9.48 (s, *Me*-im) ppm. ^{19}F NMR (282.40 MHz, 298.8 K, CD_3CN): δ = −79.5 ppm. FT-IR (solid, ATR): see the Supporting Information.

Ce(^{4Me}im$_3$tren): M.p.: 165–170 °C. ^{1}H NMR (400.1 MHz, 298.8 K, CD_3CN): δ = 18.15 (s, 3H), 10.09 (s, 6H), 5.05 (s, 3H), 4.43 (s, 9H, *Me*–im), −3.82 (s, 6H) ppm. $^{13}C\{^1H\}$ NMR (75.48 MHz, 298.8 K, CD_3CN): δ = 166.4 (s), 145.1 (s), 142.8 (s), 52.9 (s), 45.0 (s), 12.5 (s, *Me*-im) ppm. ^{19}F NMR (282.40 MHz, 298.8 K, CD_3CN): δ = −79.6 (s) ppm. Because of paramagnetism, too little information could be obtained from the 2D spectra, and no assignment of the different signals was possible. FT-IR (solid, ATR): see the Supporting Information.

Sm(^{4Me}im$_3$tren): M.p.: 150–165 °C. ^{1}H NMR (400.1 MHz, 298.8 K, CD_3CN) δ = 8.66 (s, 3H, N=C*H*), 6.68 (s, 3H), 4.01–3.85 (m, 6H, CH_2-2), 2.72 (s, 9 H, *Me*-im), 1.46 (t, *J* = 6.0 Hz, 6H, CH_2-1) ppm. $^{13}C\{^1H\}$ NMR (75.48 MHz, 298.8 K, CD_3CN):δ = 164.41 (s, N=*C*H), 139.50 (s), 137.25 (s), 135.26 (s), 59.00 (s, CH_2-1), 58.37 (s, CH_2-2), 9.95 (s, *Me*-im) ppm. ^{19}F NMR (282.40 MHz, 298.8 K, CD_3CN): δ = −79.5 ppm. FT-IR (solid, ATR): see the Supporting Information.

Lu(^{4Me}im$_3$tren): M.p.: 158–169 °C. ^{1}H NMR (400.1 MHz, 298.8 K, CD_3CN) δ = 10.49 (s, 3 H), 8.50 (s, 3H, N=C*H*), 7.64 (d, *J* = 152.7 Hz, 3H), 3.92 (t, *J* = 6.4 Hz, 6 H, CH_2-2), 3.21 (t, *J* = 6.3 Hz, 6H, CH_2-1), 2.40 (s, 9H, *Me*-im) ppm. $^{13}C\{^1H\}$ NMR (75.48 MHz, 298.8 K, CD_3CN): δ = 161.30 (s), 140.21 (s), 135.95 (s), 135.12 (s), 60.46 (CH_2-1), 56.94 (s, CH_2-2), 9.61 (s, *Me*-im) ppm. ^{19}F NMR (282.40 MHz, 298.8 K, CD_3CN): δ = −79.5 (s) ppm. FT-IR (solid, ATR): see the Supporting Information.

Y(^{5Me}pz$_3$tren): M.p.: 106–115 °C. ^{1}H NMR (400.1 MHz, 298.8 K, CD_3CN) δ = 8.35 (q, *J* = 1.6 Hz, 3 H), 6.55–6.50 (m, 3H), 3.91 (td, *J* = 6.4, 1.7 Hz, 6H), 3.20 (t, *J* = 6.4 Hz, 6H), 2.37 (d, *J* = 0.8 Hz, 9H) ppm. $^{13}C\{^1H\}$ NMR (75.48 MHz, 298.8 K, CD_3CN): δ = 161.69 (s), 149.76 (s), 145.55 (s), 120.84 (d, $^1J_{CF}$ = 319.1 Hz), 108.74 (s), 59.16 (s), 56.97 (s), 11.00 (s) ppm. ^{19} F NMR (282.40 MHz, 298.8 K, CD_3CN): δ = −79.3 (s) ppm. ^{89}Y NMR (19.61 MHz, 298.8 K, CD_3CN): δ = 45.3 ppm. FT-IR (solid, ATR): see the Supporting Information.

La(^{5Me}pz$_3$tren): M.p.: >275 °C decomp. ^{1}H NMR (400.1 MHz, 298.8 K, CD_3CN) δ = 11.70 (s, 3H, N–*H*), 8.28 (s, 3H, N=C*H*), 6.47 (s, 3H), 3.85 (t, J = 5.8 Hz, 6H, CH_2-2), 3.04 (t, *J* = 5.8 Hz, 6H, CH_2-1), 2.41 (s, 9 H, *Me*-pz) ppm. $^{13}C\{^1H\}$ NMR (75.48 MHz, 298.8 K, CD_3CN):δ = 159.51 (s), 149.98 (s, N=*C*H), 144.20 (s), 108.13 (s), 61.39 (s, CH_2-1), 60.04 (s, CH_2-2), 10.85 (s, *Me*-pz) ppm. ^{19}F NMR (282.40 MHz, 298.8 K, CD_3CN): δ = −79.6 ppm. FT-IR (solid, ATR): see the Supporting Information.

Ce(^{5Me}pz$_3$tren): M.p.: >280 °C decomp. ^{1}H NMR (400.1 MHz, 298.8 K, CD_3CN) δ = 16.25 (s, 3H), 9.19 (s, 3H), 2.51 (s, 9H, *Me*-pz), −1.08 (s, 6H, CH_2) ppm. $^{13}C\{^1H\}$ NMR (75.48 MHz, 298.8 K, CD_3CN): δ = 165.91 (s), 150.65 (s), 115.13 (s), 51.93 (s), 11.29 (s, pz-CH_3) ppm. ^{19} F NMR

(282.40 MHz, 298.8 K, CD_3CN): δ = −79.7 (s) ppm. Because of paramagnetism, too little information could be obtained from the 2D spectra, and no assignment of the different signals was possible. FT-IR (solid, ATR): see the Supporting Information.

Sm(^{5Me}pz$_3$tren): M.p.: > 300 °C decomp. ^{1}H NMR (400.1 MHz, 298.8 K, CD_3CN) δ = 8.52 (s, 3 H, N=C*H*), 6.90 (d, *J* = 0.8 Hz, 3H), 3.76 (t, *J* = 6.2 Hz, 6 H, CH_2–2), 2.33 (s, 9 H, *Me*-pz), 1.50 (t, *J* = 6.1 Hz, 6H, CH_2-1) ppm. ^{13}C{^{1}H} NMR (75.48 MHz, 298.8 K, CD_3CN): δ = 165.99 (s, N=*C*H), 153.76 (s), 144.79 (s), 108.88 (s), 58.62 (s, *C*H_2), 58.43 (s, *C*H_2), 10.82 (s, *Me*-pz) ppm. ^{19}F NMR (282.40 MHz, 298.8 K, CD_3CN): δ = −79.5 ppm. FT-IR (solid, ATR): see the Supporting Information.

Lu(^{5Me}pz$_3$tren): M.p.: > 150 °C decomp. ^{1}H NMR (400.1 MHz, 298.8 K, CD_3CN) δ = 8.48 (s, 3H, N=C*H*), 6.63 (s, 3H), 3.99 (td, *J* = 6.2, 1.6 Hz, 6H, CH_2-2), 3.24 (t, *J* = 6.2 Hz, 6H, CH_2-1), 2.41 (s, 9H, *Me*-pz) ppm. ^{13}C{^{1}H} NMR (75.48 MHz, 298.8 K, CD_3CN): δ = 163.13 (s, N=*C*H), 150.96 (s), 147.12 (s), 109.37 (s), 60.05 (s, *C*H_2-1), 57.37 (s, *C*H_2-2), 11.25 (s, *Me*-pz) ppm. ^{19}F NMR (282.40 MHz, 298.8 K, CD_3CN): δ = −79.4 ppm. FT-IR (solid, ATR): see the Supporting Information.

Y(py$_3$tren): M.p.: > 210 °C decomp. ^{1}H NMR (400.1 MHz, 298.8 K, CD_3CN) δ = 8.54 (d, J = 1.7 Hz, 3H, N=C*H*), 8.24–8.13 (m, 6H), 7.90–7.85 (m, 3H), 7.67–7.61 (m, 3H), 4.07 (td, *J* = 6.6, 1.7 Hz, 6H, CH_2-2), 3.33 (t, *J* = 6.6 Hz, 6H, CH_2-1) ppm. ^{13}C{^{1}H} NMR (75.48 MHz, 298.8 K, CD_3CN): δ = 169.18 (s, N=*C*H), 152.09 (s), 151.14 (s), 142.15 (s), 130.38 (s), 129.72 (s), 120.95 (d, $^1J_{CF}$ = 319.5 Hz), 59.15 (s, *C*H_2-1), 57.50 (s, *C*H_2-2) ppm. ^{19}F NMR (282.40 MHz, 298.8 K, CD_3CN): δ = −79.4 (s) ppm. ^{89}Y NMR (19.61 MHz, 298.8 K, CD_3CN): δ = 75.8 ppm. FT-IR (solid, ATR): see the Supporting Information.

La(py$_3$tren): M.p.: > 215 °C decomp. ^{1}H NMR (400.1 MHz, 298.8 K, CD_3CN): δ = 8.71 (s, 3H, N=C*H*), 8.51 (s, 3H), 8.12 (td, *J* = 7.7, 1.7 Hz, 3H), 7.81 (ddd, *J* = 7.6, 1.3, 0.8 Hz, 3H), 7.65 (t, *J* = 6.2 Hz, 3H), 4.01 (s, 6 H, CH_2-2), 3.15 (t, *J* = 5.7 Hz, 6H, CH_2-1) ppm. ^{13}C{^{1}H} NMR (75.48 MHz, 298.8 K, CD_3CN): δ = 167.1 (s, N=*C*H), 152.8 (s), 151.7 (s), 141.1 (s), 129.4 (s), 128.4 (s), 61.4 (s, *C*H_2-1), 60.7 (s, *C*H_2-2) ppm. ^{19}F NMR (282.40 MHz, 298.8 K, CD_3CN): δ = −79.6 (s) ppm. FT-IR (solid, ATR): see the Supporting Information.

Ce(py$_3$tren): M.p.: > 195 °C decomp. ^{1}H NMR (400.1 MHz, 298.8 K, CD_3CN): δ = 17.61 (s, br, 3H), 11.46 (s, br, 3H), 9.35 (s, br, 3H), 6.62 (s, br, 3H), −3.32 (s, br, 6H) ppm. ^{13}C{^{1}H} NMR (75.48 MHz, 298.8 K, CD_3CN): δ = 177.6 (s, br), 165.2 (s), 142.5 (s), 136.2 (s), 129.7 (s), 125.4 (s), 122.2 (s), 45.8 (s) ppm. ^{19}F NMR (282.40 MHz, 298.8 K, CD_3CN): δ = −79.3 (s) ppm. Because of paramagnetism, too little information could be obtained from the 2D spectra and no assignment of the different signals was possible. FT-IR (solid, ATR): see the Supporting Information.

Sm(py$_3$tren): M.p.: > 215 °C decomp. ^{1}H NMR (400.1 MHz, 298.8 K, CD_3CN) δ = 9.55 (s, 3H, N=C*H*), 8.58 (d, *J* = 7.6 Hz, 3H), 8.21 (t, *J* = 7.6 Hz, 3H), 6.95 (s, 3H), 4.17 (s, 3H), 3.93–3.72 (m, 6H, CH_2-1), 0.30 (s, 6 H, CH_2-2) ppm. ^{13}C{^{1}H} NMR (75.48 MHz, 298.8 K, CD_3CN): δ = 175.72 (s), 149.55 (s), 142.23 (s), 130.48 (s), 128.04 (s), 58.73 (s, *C*H_2-1), 56.31 (s, *C*H_2-2) ppm. ^{19}F NMR (282.40 MHz, 298.8 K, CD_3CN): δ = −79.4 (s) ppm. FT-IR (solid, ATR): see the Supporting Information.

Lu(py$_3$tren): M.p.: > 100 °C decomp. ^{1}H NMR (400.1 MHz, 298.8 K, CD_3CN) δ = 8.76 (s, 3H, N=C*H*), 8.30 (td, *J* = 7.7, 1.7 Hz, 3H), 8.03 (d, *J* = 7.5 Hz, 3H), 7.97 (s, 3H), 4.14 (t, *J* = 5.5 Hz, 6H, CH_2-2), 3.38 (t, *J* = 6.3 Hz, 6 H, CH_2-1) ppm. ^{13}C{^{1}H} NMR (75.48 MHz, 298.8 K, CD_3CN): δ = 170.78 (s), 152.30 (s, N=*C*H), 151.80 (s), 143.40 (s), 130.91 (s), 60.04 (s, *C*H_2-1), 57.84 (s, *C*H_2-2) ppm. ^{19}F NMR (282.40 MHz, 298.8 K, CD_3CN): δ = −79.4 (s) ppm. FT-IR (solid, ATR): see the Supporting Information.

Crystallographic details: Deposition Numbers 2253917 (for **Y(py$_3$tren)**), 2248253 (for **La(py$_3$tren)**), 2247697 (for **Ce(py$_3$tren)**), 2249127 (for **La(im$_3$tren)**), 2249126 (for **La(^{Me}im$_3$tren)**), 2262585 (for **Ce(^{Me}im$_3$tren)**), 2257464 (for **Y(^{4Me}im$_3$tren)**), 2267626 (for **Ce(^{4Me}im$_3$tren)**), 2262586 (for **Sm(^{4Me}im$_3$tren)**) and 2262654 (for **Ce(^{5Me}pz$_3$tren)**) contain the supplementary crystallographic data for this paper. These data are provided free of charge by the joint Cambridge Crystallographic Data Centre and Fachinformationszentrum Karlsruhe Access Structures service.

Supporting Information Summary

Additional references cited within the Supporting Information.[25–38] The Supporting Information also contain cyclic voltammograms, crystallographic Data, IR data, NMR spectra, details of the competition Studies, VT ^{19}F NMR spectra, further computational details, and the coordinates of the calculated structures.

Acknowledgements

Support by the Federal Ministry of Education and Research-(BMBF Project No. 02NUK059F) is gratefully acknowledged. The authors further acknowledge support by the state of Baden-Württemberg through bwHPC, the German Research Foundation(DFG) through grant no INST 40/575-1 FUGG(JUSTUS 2 cluster), and the State Research Agency of the Spanish Ministry of Science and Innovation (PID2021-126445OB–I00), and by the Gobierno de España MCIN/AEI/10.13039/501100011033 and Unión Europea "Next Generation EU"/PRTR (PDC2021-121248-I00, PLEC2021-007774 and CPP2022-009967). Open Access funding enabled and organized by Project DEAL. Open Access funding enabled and organized by Projekt DEAL.

Conflict of Interests

The authors declare no conflict of interest.

Data Availability Statement

The data that support the findings of this study are available in the supplementary material of this article.

Keywords: Extraction Ligands · Lanthanides · Nitrogen Ligand · NMR Spectroscopy · and Quantum Chemistry

[1] a) B. B. Beele, U. Müllich, F. Schwörer, A. Geist, P. J. Panak, *Procedia Chem.* **2012**, *7*, 146; b) T. Mangin, R. Schurhammer, G. Wipff, *J. Phys. Chem. B* **2022**, *126*, 2876; c) L. Xu, N. Pu, Y. Li, P. Wei, T. Sun, C. Xiao, J. Chen, C. Xu, *Inorg. Chem.* **2019**, *58*, 4420; d) A. V. Zaytsev, R. Bulmer, V. N. Kozhevnikov, M. Sims, G. Modolo, A. Wilden, P. G. Waddell, A. Geist, P. J. Panak, P. Wessling, et al., *Chem. Eur. J.* **2020**, *26*, 428.

[2] a) A. Geist, C. Hill, G. Modolo, M. R. J. St. Foreman, M. Weigl, K. Gompper, M. J. Hudson *Solvent Extr. Ion Exch.* **2006**, *24*, 463; b) F. W. Lewis, L. M. Harwood, M. J. Hudson, M. G. B. Drew, J. F. Desreux, G. Vidick, N. Bouslimani, G. Modolo, A. Wilden, M. Sypula, et al., *J. Am. Chem. Soc.* **2011**, *133*, 13093; c) M. R. J. St Foreman, M. J. Hudson, A. Geist, C. Madic, M. Weigl *Solvent Extr. Ion Exch.* **2005**, *23*, 645.

[3] a) H. H. Dam, D. N. Reinhoudt, W. Verboom, *Chem. Soc. Rev.* **2007**, *36*, 367; b) J. N. Mathur, M. S. Murali, K. L. Nash, *Solvent Extr. Ion Exch.* **2001**, *19*, 357.
[4] P. M. R. Wingering, S. Hohnstein, F. Krämer, M. E. A. Dilanas, C. Ruiz-Martínez, I. Fernández, F. Breher, *Chem. Eur. J.* **2023**, e202301529.
[5] a) M. W. Löble, P. Oña-Burgos, I. Fernández, C. Apostolidis, A. Morgenstern, O. Walter, F. Bruchertseifer, P. Kaden, T. Vitova, J. Rothe, et al., *Chem. Sci.* **2013**, *4*, 3717; b) P. Stock, E. Deck, S. Hohnstein, J. Korzekwa, K. Meyer, F. W. Heinemann, F. Breher, G. Hörner, *Inorg. Chem.* **2016**, *55*, 5254.
[6] M. Hudson, C. Madic, *European Commission, Directorate-General for Research and Innovation* **1998**.
[7] C. Brewer, G. Brewer, C. Luckett, G. S. Marbury, C. Viragh, A. M. Beatty, W. R. Scheidt, *Inorg. Chem.* **2004**, *43*, 2402.
[8] M. Mimura, T. Matsuo, Y. Motoda, N. Matsumoto, T. Nakashima, M. Kojima, *Chem. Lett.* **1998**, *27*, 691.
[9] Y. Sunatsuki, M. Sakata, S. Matsuzaki, N. Matsumoto, M. Kojima, *Chem. Lett.* **2001**, *30*, 1254.
[10] M. Wenzel, K. Wichmann, K. Gloe, K. Gloe, H.-J. Buschmann, K. Otho, M. Schröder, A. J. Blake, C. Wilson, A. M. Mills, et al., *CrystEngComm* **2010**, *12*, 4176.
[11] C. Huang Rare earth coordination chemistry *Fundamentals and applications*, Wiley, Hoboken, N.J. **2010**.
[12] a) G. Canard, S. Koeller, G. Bernardinelli, C. Piguet, *J. Am. Chem. Soc.* **2008**, *130*, 1025; b) M. G. Drew, M. R. Foreman, M. J. Hudson, K. F. Kennedy, *Inorg. Chim. Acta* **2004**, *357*, 4102.
[13] a) S. Alvarez, D. Avnir, M. Llunell, M. Pinsky, *New J. Chem.* **2002**, *26*, 996; b) S. Alvarez, *Chem. Rev.* **2015**, *115*, 13447.
[14] A. Poater, F. Ragone, R. Mariz, R. Dorta, L. Cavallo, *Chem. Eur. J.* **2010**, *16*, 14348.
[15] L. Falivene, Z. Cao, A. Petta, L. Serra, A. Poater, R. Oliva, V. Scarano, L. Cavallo, *Nat. Chem.* **2019**, *11*, 872.
[16] a) P. Stilbs, *Prog. Nucl. Magne. Reson. Spectrosc.* **1987**, *19*, 1; b) C. S. Johnson, *Prog. Nucl. Magne. Reson. Spectrosc.* **1999**, *34*, 203; c) P. S. Pregosin, E. Martínez-Viviente, P. G. A. Kumar, *Dalton Trans* **2003**, 4007; d) P. S. Pregosin, *Prog. Nucl. Magne. Reson. Spectrosc.* **2006**, *49*, 261; e) P. S. Pregosin, *Pure Appl. Chem.* **2009**, *81*, 615.
[17] C. L. Yaws (Ed.), *McGraw-Hill's AccessEngineering*, McGraw-Hill Education, McGraw Hill, New York, N.Y., **1999**.
[18] M. W. Löble, M. Casimiro, D. T. Thielemann, P. Oña-Burgos, I. Fernández, P. W. Roesky, F. Breher, *Chem. Eur. J.* **2012**, *18*, 5325.
[19] L. Lätsch, E. Lam, C. Copéret, *Chem. Sci.* **2020**, *11*, 6724.
[20] a) N. A. Piro, J. R. Robinson, P. J. Walsh, E. J. Schelter, *Coord. Chem. Rev.* **2014**, *260*, 21; b) A. N. Gaiser, C. Celis-Barros, F. D. White, M. J. Beltran-Leiva, J. M. Sperling, S. R. Salpage, T. N. Poe, D. Gomez Martinez, T. Jian, N. J. Wolford, et al., *Nat. Commun.* **2021**, *12*, 7230.
[21] D. D. Méndez-Hernández, P. Tarakeshwar, D. Gust, T. A. Moore, A. L. Moore, V. Mujica, *J. Mol. Model.* **2013**, *19*, 2845.
[22] a) F. Neese, *WIREs Comput. Mol. Sci.* **2012**, *2*, 73; b) F. Neese, *WIREs Comput Mol. Sci.* **2018**, *8*, e1327; c) F. Neese, F. Wennmohs, U. Becker, C. Riplinger, *J. Chem. Phys.* **2020**, *152*, 224108.
[23] P. Stilbs, *Prog. Nucl. Magn. Reson. Spectrosc.* **1987**, *19*, 1.
[24] H. J. V. Tyrrell, Diffusion in liquids. *A Theoretical and Experimental Study*, Butterworths, London, Boston **1984**.
[25] J. Koziskova, F. Hahn, J. Richter, J. Kožíšek, *Acta Chimica Slovaca* **2016**, *9*, 136.
[26] O. V. Dolomanov, L. J. Bourhis, R. J. Gildea, J. A. K. Howard, H. Puschmann, *J. Appl. Crystallogr.* **2009**, *42*, 339.
[27] G. M. Sheldrick, *Acta Cryst. A* **2015**, *71*, 3.
[28] G. M. Sheldrick, *Acta Cryst. A* **2008**, *64*, 112.
[29] G. M. Sheldrick, *Acta Cryst. C* **2015**, *71*, 3.
[30] a) F. Neese, F. Wennmohs, U. Becker, C. Riplinger, *J. Chem. Phys.* **2020**, *152*, 224108; b) F. Neese, *Comput. Mol. Sci.* **2018**, *8*, e1327; c) F. Neese, *Comput. Mol. Sci.* **2012**, *2*, 73.
[31] J. Tao, J. P. Perdew, V. N. Staroverov, G. E. Scuseria, *Phys. Rev. Lett.* **2003**, *91*, 146401.
[32] K. Eichkorn, F. Weigend, O. Treutler, R. Ahlrichs, *Theor. Chem. Acta* **1997**, *97*, 119.
[33] S. Grimme, J. Antony, S. Ehrlich, H. Krieg, *J. Chem. Phys.* **2010**, *132*, 154104.
[34] a) M. Namazian, C. Y. Lin, M. L. Coote, *J. Chem. Theory Comput.* **2010**, *6*, 2721; b) A. P. Davis, A. J. Fry, *J. Phys. Chem. A* **2010**, *114*, 12299.
[35] V. N. Staroverov, G. E. Scuseria, J. Tao, J. P. Perdew, *J. Chem. Phys.* **2003**, *119*, 12129.
[36] F. Weigend, R. Ahlrichs, *Phys. Chem. Chem. Phys.* **2005**, *7*, 3297.
[37] a) H. Böhrer, N. Trapp, D. Himmel, M. Schleep, I. Krossing, *Dalton Trans.* **2015**, *44*, 7489; b) P. Erdmann, J. Leitner, J. Schwarz, L. Greb, *Chem. Phys. Chem.* **2020**, *21*, 987.
[38] a) L. Lätsch, E. Lam, C. Copéret, *Chem. Sci.* **2020**, *11*, 6724; b) Y. Xing, A. K. Jindal, M. Regueiro-Figueroa, M. Le Fur, N. Kervarec, P. Zhao, Z. Kovacs, L. Valencia, P. Pérez-Lourido, R. Tripier, et al., *Chem. Eur. J.* **2016**, *22*, 16657.

Manuscript received: February 26, 2024
Accepted manuscript online: April 26, 2024
Version of record online: June 7, 2024